

Transport properties of heavy-fermion systems

Claas Grenzebach, Frithjof B. Anders, and Gerd Czycholl

Institut für Theoretische Physik, Universität Bremen, P.O. Box 330 440, D-28334 Bremen, Germany

Thomas Pruschke

Institut für Theoretische Physik, Universität Göttingen, D-37077 Göttingen, Germany

(Dated: 2 November 2006)

We calculate the temperature dependence of the transport properties of heavy-fermion systems such as resistivity, optical conductivity, thermoelectric power, the electronic part of the thermal conductivity, and the “figure of merit.” The one-particle properties of the periodic Anderson model are obtained within dynamical mean-field theory for the paramagnetic phase using Wilson’s numerical renormalization group and the modified perturbation theory as impurity solvers. We discuss the dependence of the transport properties on the band filling, valence, and Coulomb correlation U . The typical experimental findings can be reproduced and understood, in particular the temperature dependence of the resistance and the thermoelectric power and their absolute magnitude for both metallic heavy-fermion systems and Kondo insulators. For large values of U , we find a negative Seebeck coefficient $S(T)$ for an intermediate-temperature regime as observed in $S(T)$ of CeCu_2Si_2 . We analyze different estimates for possible characteristic low-temperature scales of the lattice. Our results indicate a one-parameter scaling of thermodynamic and some transport properties with a strongly occupancy-dependent scaling function. This is consistent with a strong-coupling local Fermi-liquid fixed point of the effective site governing all low-lying excitations for $T \rightarrow 0$ in the paramagnetic phase.

PACS numbers: 71.27.+a, 71.10.Fd, 72.10.-d, 72.15.-v

I. INTRODUCTION

For nearly 30 years the investigation of heavy-fermion systems (HFSs) has been one of the most fascinating and interesting fields in condensed matter physics both experimentally and theoretically.^{1,2} The heavy-fermion phenomenon exists in a number of lanthanide and actinide compounds and manifests itself in the apparent existence of quasiparticles with very large effective mass m^* at low temperatures T . This is seen already in the specific heat, the electronic part of which shows the usual linear temperature dependence $c = \gamma T$ at very low T for many metallic heavy-fermion systems but with a γ coefficient being 100–1000 times larger than in usual metals. However, this γ coefficient itself is strongly T dependent and rapidly decreases to “normal” values at higher T . Similarly, the static magnetic susceptibility $\chi(T)$ crosses over from a Curie law $\chi(T) \sim 1/T$ at high temperatures to a Pauli-type behavior for very low T : it approaches a finite value $\chi(T=0)$, which is also strongly enhanced compared to the Pauli susceptibility of normal metals; the ratio between γ and χ (Wilson ratio) is of order 1, indicating that both enhancements are caused by the same physical processes.

The heavy-fermion behavior is driven by the local moments of incompletely filled f shells of the lanthanide or actinide ions. At high temperature, the weakly coupled f electrons cause mainly incoherent and with decreasing temperature logarithmically growing spin-flip scattering for the conduction electrons. Below a characteristic temperature scale, a crossover to a coherent low-temperature phase is observed. The f electrons contribute significantly to the formation of heavy quasiparticles while their moments are dynamically screened. Some heavy-fermion compounds such as SmB_6 or $\text{Ce}_3\text{Bi}_4\text{Pt}_3$ exhibit similar behavior at high temperature, but for low T a crossover to an insulating heavy-fermion

ground state with a narrow gap at the Fermi energy is found.³ These heavy-fermion systems are termed *Kondo insulators* even though the insulating behavior is driven by Fermi volume effects. In this case, the strong correlation induces only a narrowing of the band gap rather than the insulator transition itself as in Mott-Hubbard insulators.

One particularly fascinating aspect of heavy-fermion compounds is that despite the existence of local moments they can undergo a superconducting phase transition, as observed⁴ in, e.g., CeCu_2Si_2 . In other systems magnetic phase transitions are reported, with a large variety of types of order depending on the composition.^{1,5} In the weak-coupling or local-moment regime, the local f moments tend to order antiferromagnetically, while in the Kondo regime itinerant magnetism with an incommensurate ordering vector \vec{Q} and strongly reduced ordered moments is observed.⁶ This crossover from local to itinerant magnetism has been studied in $\text{CeCu}_{(1-x)}\text{Ge}_2$ by variation of the coupling constant upon doping and has been attributed to the strongly temperature- and coupling-dependent residual quasiparticle-quasiparticle interaction.^{6,7,8,9}

In this paper, we focus on the calculation of transport properties of heavy-fermion systems in the paramagnetic phase. Characteristic information on heavy-fermion systems is obtained by measurements of the transport coefficients. The Seebeck coefficient $S(T)$, or the thermoelectric power, is often nonmonotonic, can exhibit different extrema, and even sign changes^{10,11,12,13,14,15} related to particle-hole asymmetries. Much of the recent interest in the heavy-fermion thermoelectricity is stirred by its large narrow peak at low temperatures which might be useful for solid-state cooling devices.¹⁶

For high T , the resistivity $\rho(T)$ is determined by a negative temperature coefficient, and one usually observes a logarithmic, “Kondo”-like increase of the resistivity $\rho(T)$ with decreasing T . In Kondo insulators, $\rho(T)$ crosses over from

low values to an activation behavior for smaller T , reflecting the insulating ground state. In metallic heavy-fermion systems—for example, CePd₃ (Ref. 17), CeAl₃ (Ref. 18), or CeCu₆ (Ref. 19)—a maximum is observed in $\rho(T)$ before the resistivity approaches a small residual value for $T \rightarrow 0$. At low temperatures T , $\rho(T)$ often obeys a T^2 law in such materials. The logarithmic increase of $\rho(T)$ above a characteristic low-energy scale T_{low} (for a discussion of low-energy scales see Sec. VI) is related to growing spin-flip scattering of the conduction electrons with decreasing temperature as a manifestation of the Kondo effect. Since the resistivity must vanish for $T \rightarrow 0$ in a translational-invariant system with a nondegenerate ground state, a maximum in $\rho(T)$ must connect these two regimes. The observation of a T^2 behavior well below the characteristic temperature scale T_{low} in combination with a strongly enhanced γ coefficient of the specific heat indicates the formation of a Landau Fermi-liquid by the heavy quasiparticles.

We show in a comprehensive study that the low-temperature transport properties of heavy fermions can be understood in terms of a minimalistic model of interaction between local and itinerant degrees of freedom within the dynamical mean-field theory.^{20,21} Spin-flip scattering between these degrees of freedom yields a logarithmically increasing resistivity with decreasing temperature. Our calculations reproduce the experimentally observed maximum and the T^2 behavior at low temperatures characteristic of coherent transport in the Fermi-liquid phase. The calculated optical conductivity exhibits a very narrow Drude peak and an optical excitation gap characteristic of heavy-fermion materials.²² The midinfrared peak is located in the correct frequency range but with a too narrow width compared to the experiment²² due to the lack of local crystal electric field excitations in our model.

We find very large absolute values for the thermoelectric power exceeding 150 $\mu\text{V/K}$ close to the Kondo insulator regime at temperatures of the order of T_{low} . In this case, the purely electronic figure of merit can be larger than 1. The absolute magnitude of the thermoelectric power agrees very well with the typical experimental reported values.^{10,11,12,13,14,15} The sign changes of $S(T)$ depend very sensitively on the particle-hole asymmetry and the band filling. Also in the experiment, the details of the thermoelectric power vary strongly between different materials.^{10,11,12,13,14,15}

The experimental evidence^{2,23} compiled over the past ten years also indicates that even for heavy-fermion systems with a paramagnetic ground state, the temperature dependence of the specific heat and the magnetic susceptibilities often do not agree with the predictions of Fermi-liquid theory.²⁴ Therefore, the phenomenological term “non-Fermi-liquid” was attributed to such regimes appearing in a large variety of different materials.^{2,23} Despite a tremendous experimental and theoretical effort it is, however, still not clear whether the non-Fermi-liquid effects observed in heavy-fermion compounds are related to novel low-lying nonlocal excitations in concentrated systems, true local non-Fermi-liquid physics^{25,26} or simply competing local energy scales.²⁷

The physics in heavy-fermion compounds is driven by the interaction between two distinct subsystems: localized,

strongly correlated f electrons hybridizing with extended conduction bands. The periodic Anderson model (PAM) takes these ingredients into account, comprising of spin degenerate conduction electrons, a lattice of correlated localized f electrons and a hybridization (cf. Sec. II A). The conduction electrons experience spin-flip scattering from the magnetic moments of the f shells. On the other hand, the model also accounts for the RKKY interaction between two localized magnetic moments in the particle-hole channel,^{7,8} leading to the competition between the Kondo screening and magnetic ordering.²⁸ While these qualitative aspects have been known for almost 30 years, a reliable calculation of the full phase diagram of the PAM in more than one dimension has not been possible yet.

In this work, we apply the dynamical mean-field theory^{20,21} (DMFT) mapping the PAM on an effective single impurity Anderson model²⁹ (SIAM), which becomes exact^{30,31} in the limit of infinite spatial dimension³² for lattice models of correlated electron systems. As impurity solvers for the effective SIAM we use Wilson’s numerical renormalization group³³ (NRG) for all interaction strength and the modified perturbation treatment^{34,35} (MPT) for small values of U . The NRG provides an accurate and non-perturbative description of the effective site³⁶ and yields the correct low-energy scale T_K for the SIAM (cf. Sec. V B): $T_K \propto \exp(-1/g)$, with the dimensionless coupling $g = J\rho_0(0)$, the spin-flip scattering rate J , and $\rho_0(0)$ being the density of states of the noninteracting conduction band of width D at its band center. Furthermore, the NRG provides detailed information on the possible fixed-point structure of the effective site. Compared to other possible and frequently used DMFT impurity solvers such as quantum Monte Carlo³⁷ (QMC), exact diagonalization (ED), and noncrossing-approximation^{38,39,40} (NCA), the NRG and MPT have the advantage to be applicable also for very low temperatures. This seems to be essential for the reproduction of Fermi-liquid behavior and simultaneously identifying the relevant low-temperature scale.

The transport properties are calculated in the linear response regime using Kubo formulas. They relate the quantities of interest—e.g., the frequency-dependent conductivity—to the charge and heat current-current response functions, which are two-particle Green functions. These response functions greatly simplify in any local approximation since current-operator vertex corrections vanish⁴¹ even in the presence of crystal field levels:^{41,42} only the free particle-hole propagator enters. From the f - and band-electron self-energies calculated within the DMFT-NRG and DMFT-MPT, the static conductivity is obtained from the transport integrals in the limit $\omega \rightarrow 0$, as well as the thermoelectric power $S(T)$ and the electronic part of the thermal conductivity $\kappa(T)$. Recently, a very comprehensive study of the transport properties in heavy-fermion systems as well as Kondo insulators using the local-moment approach (LMA) has been published in a series of papers by Logan and collaborators.^{43,44,45} Previously, Costi and Manini⁴⁶ investigated the low-energy scales and temperature-dependent photoemission in the $S = 1/2$ Kondo lattice model using the DMFT-NRG.

The scope of our paper is to calculate the resistivity, opti-

cal conductivity, the thermoelectric power, and the figure of merit for arbitrary interaction strength and band filling within a single approach, the DMFT-NRG. We address the question of the existence of several low-temperature scales in the periodic Anderson model which might manifest themselves in the transport properties. The quality of the DMFT-NRG calculations is critically examined by a comparison with the modified perturbation theory in the weak-coupling regime ($U \rightarrow 0$), accurately described by the DMFT-MPT.

The paper is organized as follows: In Sec. II we introduce the model and the notations as well as the DMFT and the two impurity solvers used: the NRG and MPT. In order to gain physical insight into the temperature evolution of the transport properties, we discuss the single-particle properties such as the temperature-dependent f -electron spectral function and self-energy of the PAM in Sec. III, since they directly determine the transport properties through the Kubo formulas. Section IV is devoted to the transport theory for the PAM and states explicitly equations for the different transport coefficients investigated. We report results for the transport quantities in Sec. V. The temperature dependences of the resistivity $\rho(T)$, the thermoelectric power $S(T)$, the thermal conductivity $\kappa(T)$, and the temperature and frequency dependence of the optical conductivity $\sigma(\omega, T)$ are shown for different values of U and band filling for metallic heavy-fermion systems as well as Kondo insulators. In Sec. VI we define precisely our different low-energy scales and discuss how they are linked. We conclude with a summary and outlook in Sec. VII.

II. THEORY

A. Model

As mentioned above, the Hamiltonian of the simplest version of the periodic Anderson model is given by

$$\hat{H} = \sum_{\vec{k}\sigma} \epsilon_{\vec{k}\sigma} c_{\vec{k}\sigma}^\dagger c_{\vec{k}\sigma} + \sum_{i\sigma} \epsilon_{f\sigma} \hat{n}_{i\sigma}^f + \frac{U}{2} \sum_{i\sigma} \hat{n}_{i\sigma}^f \hat{n}_{i-\sigma}^f + V \sum_{i\sigma} (f_{i\sigma}^\dagger c_{i\sigma} + c_{i\sigma}^\dagger f_{i\sigma}). \quad (1)$$

Here, $c_{\vec{k}\sigma}$ ($c_{\vec{k}\sigma}^\dagger$) destroys (creates) a conduction electron with spin σ , momentum \vec{k} and energy $\epsilon_{\vec{k}\sigma}$. The energy $\epsilon_{f\sigma}$ denotes the spin-dependent single particle f -level energy at lattice site i , $\hat{n}_{i\sigma}^f = f_{i\sigma}^\dagger f_{i\sigma}$ is the f -electron occupation operator (per site and spin), $f_{i\sigma}$ ($f_{i\sigma}^\dagger$) destroys (creates) an f electron with spin σ at site i , and U denotes the on-site Coulomb repulsion between two f electrons on the same site i . The uncorrelated conduction electrons hybridize locally with the f electrons via the matrix element V . While Eq. (1) includes possible Zeeman splitting of the energies in an external magnetic field H , we set $H = 0$ throughout the remainder of the paper and treat all properties as spin degenerate.

Even though only a single effective f level is considered, this model is quite general. It describes any heavy-fermion system with odd ground-state filling of the f shell,

for which in a strong crystal field environment the degenerate Hund's-rule ground state may be reduced to an effective spin-degenerate Kramers's doublet. In addition, charge fluctuations to even f fillings leave the f shell in crystal field singlets. The Hamiltonian contains four energy scales. The interplay between ϵ_f and U controls the average f filling as well as the local moment formation for large U and negative ϵ_f . The Anderson width $\Gamma_0 = V^2 \pi \rho_0(0)$ determines the charge fluctuation scale of the f electrons with $\rho_0(0)$ being the density of states of the noninteracting conduction band of width D at its band center.

The total filling per site, $n_{\text{tot}} = \sum_{\sigma} (\langle \hat{n}_{i\sigma}^c \rangle + \langle \hat{n}_{i\sigma}^f \rangle)$, is kept constant by a temperature-dependent chemical potential $\mu(T)$. We absorb the energy shifts into the band center ϵ_c of the conduction band, $\epsilon_{\vec{k}} = \epsilon_c + \tilde{\epsilon}_{\vec{k}}$, as well as the f level ϵ_f . For $n_{\text{tot}} = 2$ and $U = 0$, the uncorrelated system is an insulator at $T = 0$, since the lower of the two hybridized bands is completely filled. According to Luttinger's theorem a finite U of arbitrary strength does not change the Fermi volume which includes the full first Brillouin zone. As long as the ground state does not change symmetry due to a phase transition, the system remains an insulator at arbitrarily large Coulomb repulsion. Therefore, the nonmetallic ground state of Kondo insulators is not correlation induced, but it is already present for the noninteracting system and a consequence of Luttinger's theorem. For nonintegral values of n_{tot} , the paramagnetic phase of the system must be metallic.

In general, we can distinguish three different adiabatically connected regimes for $U \gg \Gamma_0$ and $\epsilon_f < 0$. In the mixed valence regime, $|\epsilon_f|/\Gamma_0 \approx 1$, the system is dominated by charge fluctuations yielding a nonintegral value of the f filling $n_f < 1$. In the stable moment regime $|\epsilon_f| \gg \Gamma_0$, the f electrons remain strongly localized and form a stable local moment, which tends to order antiferromagnetically due to the RKKY interaction mediated by the conduction electrons. These two regimes are connected by the Kondo regime for moderate ratios $|\epsilon_f|/\Gamma_0$. The competition between screening of the local moment due to the Kondo effect and the RKKY interaction makes this crossover regime the most interesting one since it can lead to long-range magnetic order of the residual magnetic moments. Spin-density-wave, metallic and superconducting ground states are observed in heavy-fermion materials¹ which are believed to be described by the Kondo regime.

B. Dynamical mean-field theory

Setting aside exact solutions in one dimension⁴⁷ using the Bethe ansatz for the Kondo lattice model, to our knowledge no exact analytical solution has been found for the model (1) with finite U . Therefore, one has to rely on suitable approximations for the PAM. An obvious first approximation is the assumption of a purely local, site-diagonal (i.e., \vec{k} -independent) self-energy, which for the PAM is even better justified than for other lattice models of correlated electron systems, as the first corrections are at least of order V^6 . Within a local self-energy approximation the complicated lattice problem can be mapped on an effective impurity problem; i.e., the

PAM can be mapped on an effective SIAM.²⁹ Such a mapping was first used already about 20 years ago in connection with applications of the NCA (Refs. 38,39,40 and 48) to the PAM.^{7,49,50,51,52} A self-consistency condition accounts for the feedback due to the propagation of electrons through the lattice. Metzner and Vollhardt³² and Müller-Hartmann⁵³ noticed that the local approximation becomes exact in the limit of infinite spatial dimensions ($d \rightarrow \infty$). The effective site can be viewed as correlated atomic problem within a time-dependent external field⁵⁴ or an effective SIAM.^{30,31,49} This defines the self-consistency condition of the DMFT which has been subject of two reviews.^{20,21} Within weak-coupling U -perturbation theory it could be shown⁵⁵ that a local, \vec{k} -independent self-energy is a good approximation for realistic dimension $d = 3$ as corrections due to intersite contributions to the self-energy are negligibly small. However, phase transitions remain mean field like in DMFT (Refs. 9, 21, and 56) since \vec{k} -dependent fluctuations are not included in a local approximation.

The following exact relations for the conduction electron Green function $G_\sigma(\vec{k}, z)$ and the f -electron Green function $F_\sigma(\vec{k}, z)$ can be obtained for the PAM (1):

$$G_\sigma(\vec{k}, z) = \left[z - \varepsilon_{\vec{k}\sigma} - \frac{|V|^2}{z - \varepsilon_{f\sigma} - \Sigma_\sigma^f(\vec{k}, z)} \right]^{-1}, \quad (2a)$$

$$F_\sigma(\vec{k}, z) = \left[z - \varepsilon_{f\sigma} - \Sigma_\sigma^f(\vec{k}, z) - \frac{|V|^2}{z - \varepsilon_{\vec{k}\sigma}} \right]^{-1}, \quad (2b)$$

where z is any complex energy off the real axis. Within a local approximation such as the DMFT, the \vec{k} -dependent f -electron self-energy $\Sigma_\sigma^f(\vec{k}, z)$ is replaced by a \vec{k} -independent $\Sigma_\sigma^f(z)$. From Eq. (2a), one defines a self-energy of the conduction electrons via

$$\Sigma_\sigma^c(z) = \frac{|V|^2}{z - \varepsilon_{f\sigma} - \Sigma_\sigma^f(z)}, \quad (3)$$

which can include a simple \vec{k} dependence through the hybridization matrix elements $|V|^2$, here taken as constant. For such a local self-energy $\Sigma_\sigma^c(z)$, the site-diagonal conduction-electron Green function G_σ can be written as a Hilbert transformation

$$G_\sigma(z) = \frac{1}{N} \sum_{\vec{k}} G_\sigma(\vec{k}, z) = D(z - \Sigma_\sigma^c(z)), \quad (4)$$

defined for arbitrary complex argument z as

$$D(z) = \int_{-\infty}^{\infty} d\varepsilon \frac{\rho_0(\varepsilon)}{z - \varepsilon}, \quad (5)$$

where $\rho_0(\omega)$ is the density of states of the noninteracting conduction electrons.

The DMFT self-consistency condition states that the site-diagonal matrix element of the f -electron Green function of the PAM must be equal to $F_{\text{loc},\sigma}(z)$ of an effective site problem

$$F_\sigma(z) = \frac{1}{N} \sum_{\vec{k}} F_\sigma(\vec{k}, z) = F_{\text{loc},\sigma}(z), \quad (6)$$

$$F_{\text{loc},\sigma}(z) = \frac{1}{z - \varepsilon_{f\sigma} - \Delta_\sigma(z) - \Sigma_\sigma^f(z)}, \quad (7)$$

with the same local f -electron self-energy $\Sigma_\sigma^f(z)$ for the lattice and the effective site. This defines the self-consistency condition for the functions $\Sigma_\sigma^f(z)$ and $\Delta_\sigma(z)$.

Given the Green functions $F_\sigma(z)$ and $G_\sigma(z)$, their spectral functions determine the local occupation numbers

$$n_f = \frac{1}{\pi} \sum_{\sigma} \int_{-\infty}^{\infty} d\omega f(\omega - \mu) \text{Im} F_\sigma(\omega - i0^+), \quad (8a)$$

$$n_c = \frac{1}{\pi} \sum_{\sigma} \int_{-\infty}^{\infty} d\omega f(\omega - \mu) \text{Im} G_\sigma(\omega - i0^+), \quad (8b)$$

where $f(\omega)$ denotes the Fermi function. Then, the total filling per site is given by $n_{\text{tot}} = n_f + n_c$. As a matter of convenience, we will perform an integral transformation such that μ is absorbed into ε_f and the band center ε_c ; all energies will be measured with respect to μ . For a given lattice filling n_{tot} , we have to adjust μ in addition to fulfill Eq. (6).

Before we will discuss the solution of the effective site, let us briefly comment on the implications of the analytical form of the conduction-electron self-energy (3). For a Fermi liquid, the imaginary part of Σ^f vanishes quadratically close to the chemical potential for $T \rightarrow 0$ —i.e., $\text{Im} \Sigma_\sigma^f(\omega - i0^+) \propto \omega^2$. At particle-hole symmetry—i.e., $n_{\text{tot}} = 2$ for a symmetric $\rho_0(\omega)$ — $\Sigma_\sigma^c(z)$ diverges like $1/z$ leading to an insulator. Away from particle-hole symmetry, the denominator remains finite and the imaginary part also must have Fermi-liquid properties $\text{Im} \Sigma_\sigma^c(\omega - i0^+) \propto \text{Im} \Sigma_\sigma^f(\omega - i0^+) \propto \omega^2$. The real part is very large, and therefore, the spectral function of $G_\sigma(z)$ as well as $F_\sigma(z)$ samples the high-energy band edges of $\rho_0(\omega)$ yielding a hybridization gap. This analytic properties must be fulfilled by any approximate solution of the DMFT self-consistency condition (6).

The low-temperature physics is determined by the temperature scale T_{low} which is only defined up to a constant factor. We will use the renormalization of the Anderson width by the quasiparticle spectral weight

$$T_0 = \Gamma_0 \left[1 - \frac{\partial \text{Re} \Sigma^f(\omega)}{\partial \omega} \Big|_{\omega, T \rightarrow 0} \right]^{-1} \quad (9)$$

as our choice of such a low-temperature scale $T_0 \propto T_{\text{low}}$ for our numerical analysis.⁴⁴ It is related to the mass enhancement $m^*/m = \Gamma_0/T_0$. We discuss other definitions of such a scale as well as the possibility of several low-temperature scales later in Sec. VI.

C. Numerical renormalization group

The Green function $F_{\text{loc},\sigma}$, Eq. (7), of the effective impurity problem can be viewed as the f -Green function of an effective SIAM,^{20,21,30,31,50}

$$\hat{H}_{\text{eff}} = \sum_{\sigma} (\epsilon_{f\sigma} - \mu) f_{\sigma}^{\dagger} f_{\sigma} + U \hat{n}_{\uparrow} \hat{n}_{\downarrow} + \sum_{\sigma} \int d\epsilon (\epsilon - \mu) d_{\sigma\epsilon}^{\dagger} d_{\sigma\epsilon} \\ + \sum_{\sigma} \int d\epsilon V \sqrt{\rho_{\text{eff}}(\epsilon)} (d_{\sigma\epsilon}^{\dagger} f_{\sigma} + f_{\sigma}^{\dagger} d_{\sigma\epsilon}), \quad (10)$$

with an energy-dependent hybridization function $\Gamma(\epsilon) = \pi V^2 \rho_{\text{eff}}(\epsilon) = \text{Im} \Delta(\epsilon - i0^+)$ describing the coupling of the f electron to a fictitious bath of “conduction electrons” created by $d_{\sigma\epsilon}^{\dagger}$ with density of states (DOS) $\rho_{\text{eff}}(\epsilon)$. The hybridization strength V is chosen to be constant, defined via

$$\pi V^2 = \int d\epsilon \Gamma(\epsilon), \quad (11)$$

and equal to V in the original model (1).

We accurately solve the Hamiltonian (10) using Wilson’s NRG.^{33,57} The key ingredient in the NRG is a logarithmic discretization of the continuous bath, controlled by the parameter³³ $\Lambda > 1$. The Hamiltonian is mapped onto a semi-infinite chain, where the N th link represents an exponentially decreasing energy scale $D_N \sim \Lambda^{-N/2}$. Using this hierarchy of scales the sequence of finite-size Hamiltonians \mathcal{H}_N for the N -site chain is solved iteratively, truncating the high-energy states at each step to maintain a manageable number of states. The reduced basis set of \mathcal{H}_N thus obtained is expected to faithfully describe the spectrum of the full Hamiltonian on the scale of D_N , corresponding³³ to a temperature $T_N \sim D_N$ from which all thermodynamic expectation values are calculated. The energy-dependent hybridization function $\Delta(z)$ determines the coefficients of the semi-infinite chain.⁵⁸

The NRG is used to calculate the spectral function of the Green function at finite temperatures. We used a slight modification of the algorithm⁵⁹ for finite temperature Green functions by Bulla *et al.*⁶⁰ with the broadening function⁶¹

$$\delta(\omega - E) \rightsquigarrow e^{-b^2/4} e^{-[\log(\omega/E)/b]^2} / (\sqrt{\pi} b |E|),$$

where we choose $b = 0.6$. As usual, the raw NRG Green functions determine the self-energy $\Sigma_{\sigma}^f(z)$ by the exact ratio

$$\Sigma_{\sigma}^f(z) = U \frac{M_{\sigma}^{\text{NRG}}(z)}{F_{\text{loc}}^{\text{NRG}}(z)}, \quad (12)$$

derived via equation of motion technique,⁶¹ where $M_{\sigma}^{\text{NRG}}(z) = \langle\langle f_{\sigma} f_{-\sigma}^{\dagger} f_{-\sigma} | f_{\sigma}^{\dagger} \rangle\rangle(z)$.

D. Modified perturbation theory

The MPT is an approximation for calculating the self-energy of the SIAM starting from the following ansatz:

$$\Sigma_{\sigma}^f(z) = U n_{-\sigma}^f + \frac{\Sigma_{\sigma}^{(2)}(z)}{1 - \beta_{\sigma} \Sigma_{\sigma}^{(2)}(z)}. \quad (13)$$

It is based on second-order perturbation theory⁶² (SOPT) relative to Hartree-Fock solution with U as expansion parameter.

Here, $\Sigma_{\sigma}^{(2)}$ is the second-order contribution to the self-energy (choosing $\beta_{\sigma} = 0$ reproduces the SOPT),

$$\Sigma_{\sigma}^{(2)}(z) = U^2 \iiint \frac{\rho_{\sigma}^{\text{HF}}(\omega_1) \rho_{-\sigma}^{\text{HF}}(\omega_2) \rho_{-\sigma}^{\text{HF}}(\omega_3)}{z - \omega_1 + \omega_2 - \omega_3} \\ \times \{f(\omega_1)[1 - f(\omega_2)]f(\omega_3) \\ + [1 - f(\omega_1)]f(\omega_2)[1 - f(\omega_3)]\} d\omega_1 d\omega_2 d\omega_3, \quad (14)$$

with the Hartree-Fock f -electron spectral functions of the effective SIAM:

$$\rho_{\sigma}^{\text{HF}}(\omega) = -\frac{1}{\pi} \text{Im} \frac{1}{\omega + i0^+ + \tilde{\mu} - \epsilon_{f\sigma} - U n_{-\sigma}^f - \Delta_{\sigma}(\omega + i0^+)}. \quad (15)$$

The parameter β_{σ} is constructed such that the exactly solvable atomic limit $V = 0$ as well as the first four spectral moments are correctly reproduced.^{34,35} The Hartree-Fock f occupation must equal the full f occupation $n_{-\sigma}^f$ determining the effective Hartree-Fock chemical potential $\tilde{\mu}$.

III. RESULTS FOR THE SINGLE-PARTICLE DYNAMICS

All transport calculations rely on the results for the single-particle Green functions of the PAM. We use a Gaussian model density of states for the unperturbed conduction-electron system—i.e., $\rho_0(\omega) = \exp[-(\omega/t^*)^2/2]/(t^*\sqrt{2\pi})$ —which is appropriate for a d -dimensional hypercubic lattice in the limit $d \rightarrow \infty$.³² In the following, we measure energies in units of $\Gamma_0 = \pi V^2 \rho_0(0)$ —i.e., the hybridization is fixed at $V^2 = 2t^* \Gamma_0 / \sqrt{2\pi}$ —and choose $\sqrt{2}t^* = 10\Gamma_0$. As impurity solvers, we use the NRG as well as the MPT. The chemical potential μ has to be determined self-consistently for a given total number of electrons, n_{tot} , per site; in the following figures, energies (frequencies) are measured relative to the chemical potential μ —i.e., we have $\mu = 0$ and the band center ϵ_c is shifted accordingly.

A. f -electron spectral function and self-energy at finite temperature T

Using the NRG the calculation of the spectral functions for finite T is numerically very challenging. In contrast to the spectral functions^{36,61} at $T = 0$, where only the ground-state excitations are relevant, all excitations contribute according to their statistical weight, but the NRG only provides spectral information up to an energy scale $\omega_N \propto \Lambda^{-N/2}$. While the number of NRG iterations, N , is in principal arbitrary and arbitrary small excitations could be resolved, Wilson has already pointed out³³ that the lowest energy scale ω_N should be identified with the temperature T for which thermodynamical expectation values are calculated. It is obvious from the Lehmann representation of the spectral function that eigenstates of the Hamiltonian with eigenenergies $E_M < T$ contribute equally to the spectral functions. Therefore, we stop the NRG iteration when $\omega_N \approx T$ and must interpolate for frequencies $|\omega| < \omega_N$. The technical details of our

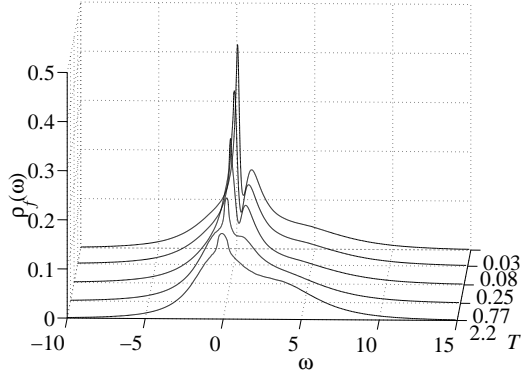


FIG. 1: f -DOS $\rho_f(\omega)$ calculated with DMFT-NRG for $U/\Gamma_0 = 5$, $\varepsilon_f - \varepsilon_c = -2.5\Gamma_0$, chemical potential $\mu = 0$, and a filling $n_{\text{tot}} = 1.6$ at several finite temperatures T/Γ_0 . NRG parameters: number of retained NRG states, $N_s = 1500$, $\Lambda = 1.6$, $\delta/\Gamma_0 = 10^{-3}$.

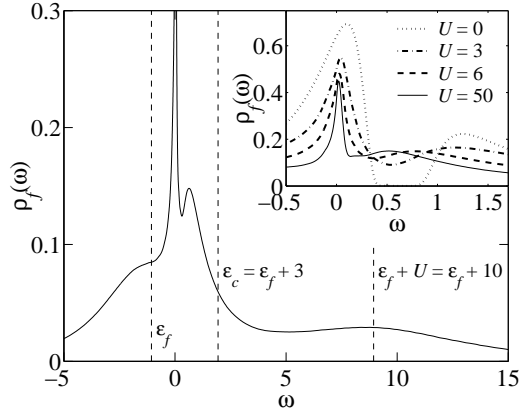


FIG. 2: f -DOS $\rho_f(\omega)$ calculated with DMFT-NRG for $U/\Gamma_0 = 10$, $\varepsilon_f - \varepsilon_c = -3\Gamma_0$, chemical potential $\mu = 0$, filling $n_{\text{tot}} = 1.6$, and finite temperature $T = 0.0003\Gamma_0$. A three-peak structure with peaks at ε_f , μ , and $\varepsilon_f + U$ is visible. In the inset the transition from a hybridization gap for $U = 0$ (exact result) to a pseudogap for $U/\Gamma_0 \in \{3, 6, 50\}$ is shown. NRG parameters: as in Fig. 1.

finite-temperature algorithm are described in the Appendix of Ref. 59; other possible approaches are found in Refs. 60 and 63,64,65.

An exemplary series of f -spectral functions $\rho_f(\omega)$ calculated with DMFT-NRG for different temperatures T and fixed $U = 5\Gamma_0$ is shown in Fig. 1 for the metallic regime with a filling $n_{\text{tot}} = 1.6$ and $\varepsilon_f - \varepsilon_c = -2.5\Gamma_0$. A hybridization pseudogap develops close to the chemical potential $\mu = 0$ for T decreasing below a characteristic temperature T_{low} . The moderate value of U leads to a spectrum where the high-energy charge excitations are not well separated from the resonance close to the chemical potential.

The typical structure of the f -spectral function $\rho_f(\omega)$ calculated with DMFT-NRG for a larger value of $U/\Gamma_0 = 10$, $\varepsilon_f - \varepsilon_c = -3\Gamma_0$, at a temperature $T = 0.0003\Gamma_0$ well below T_{low} is depicted in Fig. 2 (a detailed discussion of possible estimates for T_{low} is found in Sec. VI). A pronounced peak structure with a pseudogap dominates the low-energy part of

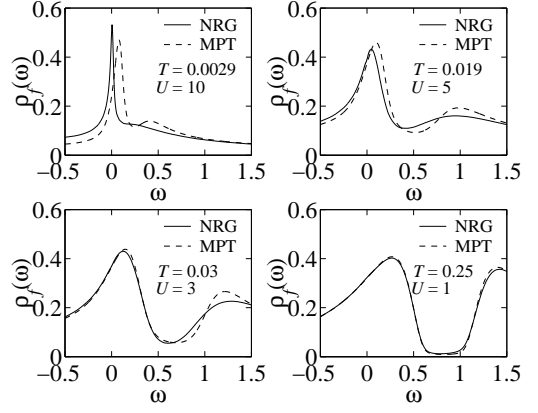


FIG. 3: Comparison between the f -DOS $\rho_f(\omega)$ calculated with DMFT-NRG and DMFT-MPT for $U/\Gamma_0 \in \{10, 5, 3, 1\}$ and $\varepsilon_f - \varepsilon_c = -U/2$ at finite temperatures T/Γ_0 as indicated. Here, the chemical potential is $\mu = 0$ with filling $n_{\text{tot}} = 1.6$. NRG parameters: as in Fig. 1.

the spectrum in the vicinity of the chemical potential similar to the one shown in Fig. 1. In addition, we observe two shallow high-energy peaks, one at ε_f below μ , one at $\varepsilon_f + U$ which corresponds to double occupancy of the f levels. It is always correctly positioned by the NRG, independent of the value of U , but with a linewidth too large due to the NRG broadening procedure (see Refs. 59 and 61 for details).

In the inset of Fig. 2 the development of the hybridization gap of the f -spectral function $\rho_f(\omega)$ with increasing $U > 0$ is shown and compared with the exact result for $U = 0$. For $U = 0$, we obtain from an uncorrelated hybridized band a hybridization gap above $\mu = 0$ of a width $\propto V$. It arises from the divergence of the real part of $\Sigma_\sigma^c(z \rightarrow \varepsilon_f)$ given in Eq. (3): the high-energy part of the free density of states ρ_0 defines the shape of the gap via the exact relation between G_σ and F_σ ,

$$F_\sigma(z) = \frac{\Sigma_\sigma^c(z)}{V^2} \{1 + \Sigma_\sigma^c(z)D[z - \Sigma_\sigma^c(z)]\}. \quad (16)$$

For a DOS $\rho_0(\omega)$ of Gaussian shape the hybridization gap is, strictly speaking, only a pseudogap even at $U = 0$. A real gap only arises for densities of states with well-defined sharp band edges such as a semielliptical or a true finite- d DOS. However, with increasing U the gap will always evolve into a pseudogap anyway due to the finite lifetime of the quasiparticles, reflected in the growing imaginary part of $\Sigma_\sigma^f(\omega)$. This effect is clearly seen in the inset to Fig. 2. The width of the pseudogap and of the whole Kondo resonance peak structure is decreasing with increasing U stemming from the reduction of the quasiparticle weight at the chemical potential.

A comparison of the f -spectral functions for finite T obtained in DMFT-NRG and DMFT-MPT for $\varepsilon_f - \varepsilon_c = -U/2$ and $n_{\text{tot}} = 1.6$ (metallic case) and four different values of U is displayed in Fig. 3. Again, only a pseudogap is found at finite U which is narrowing with increasing U . As expected, the DMFT-MPT curves agree very well with the DMFT-NRG graphs for small U . This is not surprising, because the MPT is based on U -perturbation theory and must, therefore, become

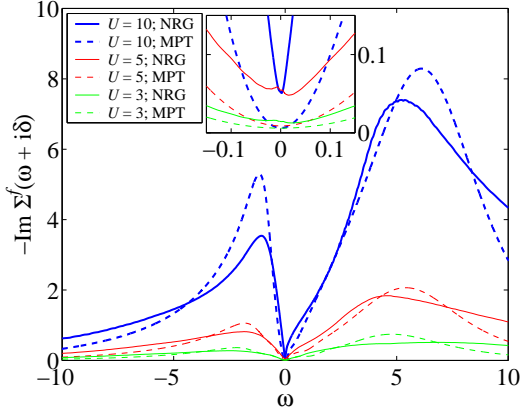


FIG. 4: (Color online) Comparison between the self-energy $\Sigma^f(\omega)$ in DMFT-NRG and DMFT-MPT for $U/\Gamma_0 \in \{3, 5, 10\}$. The inset shows a close-up of the vicinity of $\mu = 0$. All parameters are as in Fig. 3, in particular finite temperatures $T/\Gamma_0 \in \{0.03, 0.019, 0.0029\}$.

correct for sufficiently small U . Already for $U/\Gamma_0 = 5$, however, one observes deviations between the MPT and NRG approaches. For $U/\Gamma_0 = 10$ ($U/\sqrt{2}t^* = 1$) the width of the resonance peak at the Fermi energy is obviously too large in MPT; i.e., quantitatively there is a strong overestimation of the low-energy scale within DMFT-MPT. For large U the MPT cannot reproduce the correct Kondo temperature scale, as the physics in this regime is driven by the spin-flip scattering J proportional to $1/U$ and is, therefore, nonperturbative in U .

Figure 4 shows the frequency dependence of the (imaginary part of the) f -electron self-energy obtained in DMFT-NRG and DMFT-MPT, corresponding to Fig. 3. Here, the imaginary part of the self-energy is finite even at $\omega = 0$, and away from the chemical potential one observes a quadratic $(\omega - \mu)^2$ behavior as expected for Fermi liquids. The finite value at $\omega = \mu = 0$ is not only due to the finite T , but it has also a contribution from a finite imaginary part δ (i.e., an additional Lorentzian broadening), which we had to introduce for numerical reasons. As we observed numerical instabilities in the self-consistency equations (6) and (7) as well as inaccuracies in the local self-energy (12) in NRG, we solved the set of equations (6) and (7) in the complex plane at a finite shift $\delta/\Gamma_0 = 10^{-3}$ away from the real axis to obtain stable numerical solutions. Physically this artificial broadening δ can be interpreted to simulate the effects of impurity scattering, yielding a finite lifetime corresponding to a finite imaginary part of an additional “disorder” self-energy. But one also sees from Fig. 4 that—in spite of the same small imaginary part δ —the MPT result for $\text{Im}\Sigma^f(0)$ is systematically smaller than the NRG result, even for small U . This is an indication that the finite value in NRG is not only caused by the temperature offset and δ but also by the additional Gaussian broadening^{59,61} described in Sec. II C and additional numerical errors stemming from the relation (12) to determine the self-energy in NRG at finite temperature.

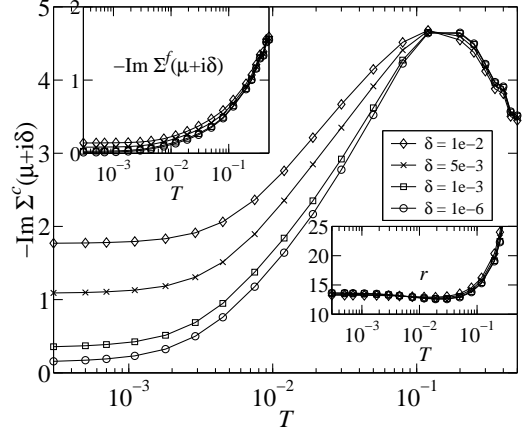


FIG. 5: Influence of the shift δ on $\text{Im}\Sigma^c(\mu, T)$ for $U/\Gamma_0 = 10$, $\varepsilon_f - \varepsilon_c = -U/2$, and $n_{\text{tot}} = 1.6$. The ratio $r = V^2 / [\varepsilon_f + \text{Re}\Sigma^f(0)]^2$ (right inset) is almost constant for low T , here $r \approx 14 \gg 1$. This leads to the enhancement of $\text{Im}\Sigma^c(\mu, T)$ for low T compared to $\text{Im}\Sigma^f(\mu, T)$ as shown in the left inset. NRG parameters as in Fig. 1.

B. Temperature dependence of band-electron self-energy $\Sigma^c(\omega)$

Since the conduction-electron self-energy $\Sigma^c(\omega, T)$ strongly influences the transport properties of the PAM, we study its imaginary part at $\omega = 0$ —i.e., the conduction-electron scattering rate. According to Eq. (3), it is given by

$$\text{Im}\Sigma_\sigma^c(0) = \frac{|V|^2 \text{Im}\Sigma_\sigma^f(0)}{[\varepsilon_{f\sigma} + \text{Re}\Sigma_\sigma^f(0)]^2 + [\text{Im}\Sigma_\sigma^f(0)]^2}. \quad (17)$$

Analytically, we can distinguish two cases.

(i) If $|\varepsilon_{f\sigma} + \text{Re}\Sigma_\sigma^f(0)| \ll |\text{Im}\Sigma_\sigma^f(0)|$, the conduction-electron scattering rate is reciprocal proportional to the f -electron scattering rate—i.e., $\text{Im}\Sigma_\sigma^c(0) \approx V^2 / \text{Im}\Sigma_\sigma^f(0)$. This is the case for the Kondo insulator regime, where $\varepsilon_{f\sigma} + \text{Re}\Sigma_\sigma^f(0) \rightarrow 0$.

(ii) Only when $|\varepsilon_{f\sigma} + \text{Re}\Sigma_\sigma^f(0)| \gg |\text{Im}\Sigma_\sigma^f(0)|$ is the denominator of Eq. (17) dominated by the real part $[\varepsilon_{f\sigma} + \text{Re}\Sigma_\sigma^f(0)]^2$ and the c -scattering rate becomes proportional to $|\text{Im}\Sigma_\sigma^f(0)|$.

We show the temperature dependence of the c -electron scattering rate and its dependence on δ for a fixed value of $U/\Gamma_0 = 10$ in Fig. 5. While the f -electron scattering rate remains very small for low T (cf. left inset of Fig. 5), the c -electron scattering rate has a much larger finite $T \rightarrow 0$ value. This originates from the small but finite imaginary part of the conduction-electron self-energy (17) as a consequence of the small (artificial) imaginary part δ , here $\delta/\Gamma_0 \in \{10^{-2}, 5 \times 10^{-3}, 10^{-3}, 10^{-6}\}$ and the numerical error in the ratio of two Hilbert transformed spectral functions in Eq. (12). The small finite $|\text{Im}\Sigma_\sigma^f(0)|$ is enhanced if the ratio $r := V^2 / [\varepsilon_{f\sigma} + \text{Re}\Sigma_\sigma^f(0)]^2$ is larger than 1, as it is usually the case since the hybridization gap is very close to the chemical

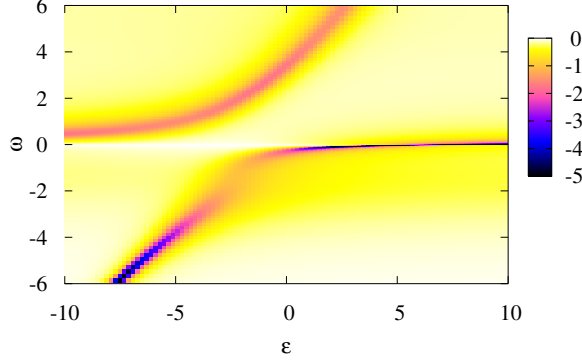


FIG. 6: (Color online) Contour plot of the total energy-dependent density of state $\rho(\varepsilon, \omega) = \rho_f(\varepsilon, \omega) + \rho_c(\varepsilon, \omega)$ for $U/\Gamma_0 = 8$, $\varepsilon_f - \varepsilon_c = -U/2$, $n_{\text{tot}} = 1.6$, $\mu = 0$, $T/\Gamma_0 = 3 \times 10^{-4}$. NRG parameters: as in Fig. 1.

potential, and $-\varepsilon_{f\sigma} - \text{Re}\Sigma_\sigma^f(0)$ is an estimate for its location. As one can see from the right inset of Fig. 5, we indeed have a ratio $r \gtrsim 14 > 1$. Therefore, we can estimate the c -electron scattering rate by

$$\text{Im}\Sigma_\sigma^c(0) \sim 14\text{Im}\Sigma_\sigma^f(0)$$

for the chosen parameters $U/\Gamma_0 = 10$ and $n_{\text{tot}} = 1.6$, which explains why the artificial finite imaginary part is even more important and pronounced for $\text{Im}\Sigma_\sigma^c(0)$ than it is for $\text{Im}\Sigma_\sigma^f(0)$.

C. Renormalized band structure

In the previous section, Sec. III A, we presented the local, or \vec{k} -summed spectral function. In the Fermi-liquid phase of the model, new quasiparticles are formed as a mixture of f and c degrees of freedom. The resulting renormalized band structure can be visualized by plotting the energy $\varepsilon = \varepsilon_{\vec{k}}$ and frequency dependent density of states $\rho(\varepsilon, \omega) = \rho_f(\varepsilon, \omega) + \rho_c(\varepsilon, \omega)$, where

$$\rho_f(\varepsilon, \omega) = \text{Im}F_\sigma(\varepsilon, \omega - i0^+)/\pi, \quad (18a)$$

$$\rho_c(\varepsilon, \omega) = \text{Im}G_\sigma(\varepsilon, \omega - i0^+)/\pi, \quad (18b)$$

as a two-dimensional (2D) color (online) contour plot displayed in Fig. 6. For $n_{\text{tot}} = 1.6$, the chemical potential $\mu = 0$ lies at the top of the lower hybridized band. For $V = 0$, we would have a sharp line at $\omega = \varepsilon - \varepsilon_c$ with purely c character, while two lines with fractional weight of $1/2$ at $\omega = \varepsilon_f = \varepsilon_c - U/2$ and $\omega = \varepsilon_f + U = \varepsilon_c + U/2$ with f character could be found. At finite V , the f electrons become part of the Fermi volume. Indeed, the almost dispersionless and therefore heavy quasiparticles close to the chemical potential have mainly f character. The second band is located above the chemical potential. We note—not shown here—that this renormalized band picture remains valid even well above the low-temperature scale. The dark colored peaks of $\rho(\varepsilon, \omega)$ are

broadened by the increasing imaginary part of the self-energy but can still be traced by the zeros of the real part of the reciprocal Green functions $G_\sigma(\varepsilon, \omega)$ and $F_\sigma(\varepsilon, \omega)$. This observation turns out to be very important to understand the midinfrared peak in the optical conductivity.^{22,66}

IV. TRANSPORT THEORY

To describe the electronic transport within the PAM we start from the standard relations for the generalized transport coefficients, according to which the electrical current density \vec{J} and the heat current density \vec{q} depend linearly on the electric field \vec{E} and the temperature gradient ∇T :

$$\vec{J} = L_{11}\vec{E} + L_{12}\left(-\frac{1}{T}\nabla T\right), \quad (19a)$$

$$\vec{q} = L_{21}\vec{E} + L_{22}\left(-\frac{1}{T}\nabla T\right). \quad (19b)$$

All coefficients are calculated within the linear response approach, starting from similar Kubo formulas.^{67,68} For symmetry reasons, $L_{12} = L_{21}$ holds.

For example, the real part of the frequency dependent (optical) conductivity tensor^{68,69,70} $\sigma(\omega) = L_{11}(\omega)$ is related to the current-current correlation function and written as

$$\sigma_{\alpha\beta}(\omega) = -\frac{1}{\omega N V_0} \text{Im}\langle\langle j_\alpha | j_\beta^\dagger \rangle\rangle(\omega + i0^+), \quad (20)$$

where $V_0 = a^3$ is the volume of the unit cell and N counts the number of lattice sites. It has been shown⁷¹ that the current operator of the PAM has two contributions: a conduction-electron part and a part proportional to $\nabla V_{\vec{k}}$. The f electrons do not appear in the current, since they do not disperse. For a \vec{k} -independent hybridization, only the conduction electrons carry the electrical and heat currents:

$$\vec{J} = e \sum_{\vec{k}\sigma} \vec{v}_{\vec{k}} c_{\vec{k}\sigma}^\dagger c_{\vec{k}\sigma}, \quad (21)$$

where $\vec{v}_{\vec{k}} = \frac{1}{\hbar} \nabla_{\vec{k}} \varepsilon_{\vec{k}}$ is the group velocity. Hence, the current-susceptibility tensor $\langle\langle \vec{J} | \vec{J}^\dagger \rangle\rangle(z)$ is connected to the particle-hole Green function

$$\langle\langle \vec{J} | \vec{J}^\dagger \rangle\rangle(z) = e^2 \sum_{\sigma\sigma' \vec{k}\vec{k}'} \vec{v}_{\vec{k}} \vec{v}_{\vec{k}'}^T \langle\langle c_{\vec{k}\sigma}^\dagger c_{\vec{k}\sigma} | c_{\vec{k}'\sigma'}^\dagger c_{\vec{k}'\sigma'} \rangle\rangle(z). \quad (22)$$

In a cubic crystal, the conductivity is isotropic: $\sigma_{\alpha\beta}(\omega) = \sigma(\omega)\mathbb{1}$. From now on, we will consider only the xx -component of the conductivity $\sigma(\omega) \equiv \sigma_{xx}(\omega)$.

In general, the full two-particle Green function $\langle\langle c_{\vec{k}\sigma}^\dagger c_{\vec{k}\sigma} | c_{\vec{k}'\sigma'}^\dagger c_{\vec{k}'\sigma'} \rangle\rangle(z)$ involves vertex corrections which reflect residual particle-particle interactions.⁶⁸ However, in the limit $d \rightarrow \infty$ it was shown that current operator vertex corrections vanish.^{72,73} Thus, it is consistent with the DMFT assumption of a \vec{k} -independent self-energy that these vertex corrections vanish for any lattice model of correlated electron systems. For the special case of a local approximation for the

PAM this was already shown in Refs. 41, 42, and 74, as for symmetry reasons

$$\sum_{\vec{k}} \vec{v}_{\vec{k}} |V_{\vec{k}}|^2 G_{\vec{k}}(z + \omega) G_{\vec{k}}(z) = 0.$$

Therefore, we obtain

$$\begin{aligned} \langle \langle j_x | j_x^\dagger \rangle \rangle (\omega + i0^+) &= \frac{e^2}{\hbar^2} \sum_{\vec{k}\sigma} \left(\frac{\partial \varepsilon_{\vec{k}}}{\partial k_x} \right)^2 \int_{-\infty}^{\infty} d\omega' f(\omega') \rho_c(\varepsilon_{\vec{k}}, \omega') \\ &\times [G_{\sigma}(\vec{k}, \omega' + \omega + i0^+) \\ &+ G_{\sigma}(\vec{k}, \omega' - \omega - i0^+)]. \end{aligned} \quad (23)$$

Within the DMFT, the lattice one-particle Green function depends only on the (complex) energy z and bare band dispersion $\varepsilon_{\vec{k}}$: $G_{\sigma}(\vec{k}, z) = G_{\sigma}(\varepsilon_{\vec{k}}, z)$. Then

$$\frac{1}{N} \sum_{\vec{k}} \left(\frac{\partial \varepsilon_{\vec{k}}}{\partial k_x} \right)^2 A(\varepsilon_{\vec{k}}) = \int_{-\infty}^{\infty} d\varepsilon \tilde{\rho}_0(\varepsilon) A(\varepsilon), \quad (24)$$

with

$$\tilde{\rho}_0(\varepsilon) = \frac{1}{N} \sum_{\vec{k}} \left(\frac{\partial \varepsilon_{\vec{k}}}{\partial k_x} \right)^2 \delta(\varepsilon - \varepsilon_{\vec{k}}). \quad (25)$$

$\tilde{\rho}_0(\varepsilon)$ has been evaluated approximately in large dimensions⁷⁵ as

$$\tilde{\rho}_0(\varepsilon) = \frac{(at^*)^2}{d} \rho_0(\varepsilon) + O(1/d^2) \quad (26)$$

on a hyper-cubic lattice. Then, Eq. (23) can be reduced to a sum of Hilbert transforms, defined in Eq. (5).

By taking the limit $\omega \rightarrow 0$ in Eq. (23), the static conductivity $\sigma = L_{11}$ is obtained, and we get for the generalized transport coefficients:

$$L_{11} = \frac{e^2}{\hbar a} \int_{-\infty}^{\infty} [-f'(\omega)] \tau(\omega) d\omega, \quad (27a)$$

$$L_{12} = \frac{e}{\hbar a} \int_{-\infty}^{\infty} [-f'(\omega)] (\omega - \mu) \tau(\omega) d\omega, \quad (27b)$$

$$L_{22} = \frac{1}{\hbar a} \int_{-\infty}^{\infty} [-f'(\omega)] (\omega - \mu)^2 \tau(\omega) d\omega. \quad (27c)$$

Here $\tau(\omega)$ represents a generalized relaxation time defined as

$$\tau(\omega) = \frac{2\pi}{d} (t^*)^2 \int_{-\infty}^{\infty} \rho_0(\varepsilon) \rho_c^2(\varepsilon, \omega) d\varepsilon \quad (28)$$

and $f'(\omega)$ is the derivative of the Fermi function. Only in the Fermi-liquid regime does one have $\tau(\omega) \propto 1/\text{Im}\Sigma_c(\omega + i0^+)$ and the linearized Boltzmann transport theory is recovered.

The thermal conductivity κ and the thermoelectric power S are then given by^{68,70}

$$S = \frac{1}{T} \frac{L_{12}}{L_{11}} = \frac{k_B}{|e|} \frac{|L_{12}|}{k_B T L_{11}}, \quad (29)$$

$$\kappa = \frac{1}{T} \left(L_{22} - \frac{L_{12}^2}{L_{11}} \right). \quad (30)$$

The thermoelectric power S is defined as the proportional constant between an applied temperature gradient and the measured voltage drop in the absence of a current flow. The Peltier coefficient given by the ratio of heat and electrical current is related to the thermoelectric power by $\Pi = TS$. Note that $|e|L_{12}/k_B T L_{11}$ is dimensionless and $k_B/|e| \approx 86 \mu\text{V/K}$. Therefore, the thermoelectric power is given in absolute units; only the scale of temperature axis must be fixed by experiment.

If we assume one electron per unit cell of the volume a^3 , $a = 10^{-10} \text{ m}$, the resistivity $\rho = \sigma^{-1}$ has the natural unit

$$\sigma_0^{-1} = \hbar a / e^2 \approx 41 \mu\Omega \text{ cm}. \quad (31)$$

Similarly, if we assume $\Gamma_0 = 100 \text{ meV}$, the thermal conductivity is given in units of

$$\frac{k_B \Gamma_0}{\hbar a} \approx 0.21 \text{ W/(K cm)}. \quad (32)$$

Finally, the dimensionless figure of merit is defined as

$$ZT = \frac{T \sigma S^2}{\kappa}, \quad (33)$$

which measures the efficiency of a thermoelectric material.

V. RESULTS FOR THE TRANSPORT PROPERTIES

A. Resistivity

The (static or direct current) resistivity $\rho(T)$ is obtained from the reciprocal of $\sigma(T)$, Eq. (27a). To achieve better convergence of the DMFT equation at low temperatures again a finite offset $\delta > 0$ from the real axis was introduced. As discussed in Sec. III A, the NRG provides accurate spectral functions only for frequencies $\omega \geq T$. In the linear-response transport-integrals (27), however, only the low-frequency spectral information in the Fermi window $|\omega| < 2T$ contributes. This intrinsic property of the NRG makes it very difficult to obtain reliable spectral information for low frequencies at finite temperatures needed for calculating transport properties.

In Fig. 7, the resistivity is displayed for fixed filling $n_{\text{tot}} = 1.6$, $U/\Gamma_0 = 10$, $\sqrt{2}t^* = 10\Gamma_0$ and various values of the shift δ as in Fig. 5. Physically, a finite δ can be interpreted as simulating the effects of lattice defects and/or of a small but finite concentration c of nonmagnetic impurities giving rise to a finite “impurity self-energy” imaginary part (inverse scattering time) $\delta \sim c$, which leads to a finite residual resistivity for $T \rightarrow 0$. Figure 7 shows that the residual resistivity $\rho(T=0)$ is, in fact, increasing with increasing δ . As discussed already in Sec. III B, the finite imaginary part of the conduction-electron self-energy (17) is much enhanced compared to the imaginary part of the f -electron self-energy, which explains the strong dependence on δ seen in Fig. 7. However, even in the limit $\delta \rightarrow 0$ a finite $\rho(T=0)$ is obtained for $T \rightarrow 0$ in DMFT-NRG. Not only the finite δ but also the additional Gaussian broadening and the limited accuracy of the NRG in the regime $\omega < T$

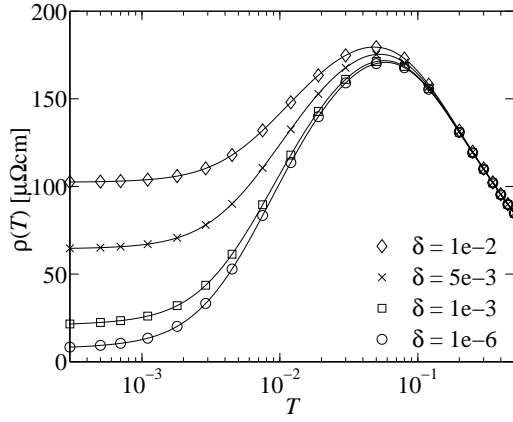


FIG. 7: Influence of the shift δ on the static resistivity in DMFT-NRG for $U/\Gamma_0 = 10$, $\varepsilon_f - \varepsilon_c = -U/2$, and $n_{\text{tot}} = 1.6$. All parameters are as in the corresponding Fig. 5.

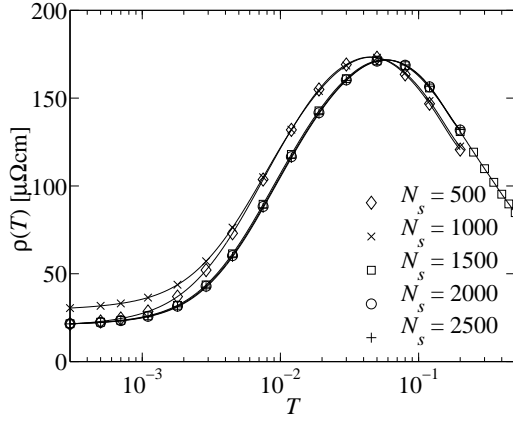


FIG. 8: Resistivity $\rho(T)$ obtained in DMFT-NRG for different number of kept states N_s and fixed values of $\delta/\Gamma_0 = 10^{-3}$ and $\Lambda = 1.6$. Other parameters as in Fig. 7.

causes the finite self-energy imaginary part and the finite $\rho(0)$. We reproduce the typical metallic HFS behavior^{17,18,19} within our DMFT-NRG treatment: a resistivity increasing with increasing T for low T , a maximum of the order $100 \mu\Omega \text{ cm}$ at a characteristic temperature T_{max} (about 10–200 K), and a $\rho(T)$ (logarithmically) decreasing with increasing T for $T > T_{\text{max}}$.

For the same parameters as in Fig. 7 the dependence of $\rho(T)$ on the NRG parameter N_s (number of states kept) is shown in Fig. 8. One observes that for $N_s \geq 1500$, $\rho(T)$ no longer depends on N_s . Therefore, all further DMFT-NRG calculations have been performed for this $N_s = 1500$.

For fixed $\delta/\Gamma_0 = 10^{-3}$, a total filling $n_{\text{tot}} = 1.6$, a difference between the band center ε_c and ε_f of $\varepsilon_f - \varepsilon_c = -U/2$ and several small values of U the DMFT-NRG and DMFT-MPT results for $\rho(T)$ are compared in Fig. 9. One observes that in the high-temperature regime both results agree and that the overall agreement becomes the better the smaller U is, as expected already from our discussion in Sec. III A, Fig. 3. But for the same small δ the residual resistivity $\rho(0)$ in DMFT-MPT is much smaller than in DMFT-NRG. In DMFT-MPT

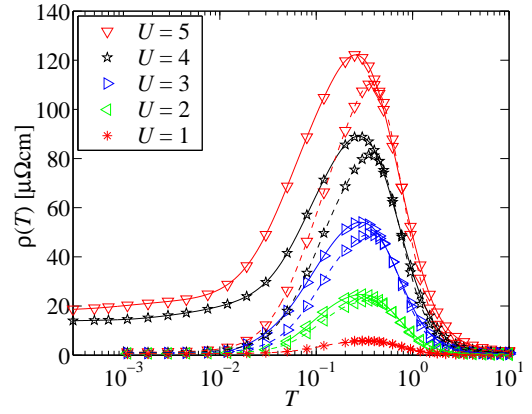


FIG. 9: (Color online) Comparison between the resistivity $\rho(T)$ in DMFT-NRG (solid lines) and DMFT-MPT (dashed lines). for different U , $\varepsilon_f - \varepsilon_c = -U/2$, and fixed total filling $n_{\text{tot}} = 1.6$ (metallic case). NRG Parameters: as in Fig. 1.

the finite $\rho(0)$ is solely determined by the finite δ whereas in DMFT-NRG the additional broadening and numerical inaccuracies at very small ω contribute.

For the same parameter set, but higher values of the correlation U , DMFT-NRG resistivity results are plotted in Fig. 10. The temperature T_{max} , at which the resistivity has its maximum, is shifted to lower values for increasing U ; as discussed in Sec. VI one obtains an exponential dependency of T_{max} on U . For sufficiently strong U the peak height at T_{max} is nearly U independent. This is seen once more from Fig. 10(b), which shows the scaling properties plotting the resistivity $\rho(T) - \rho(T_0/100)$ versus T/T_0 [for the low-temperature scale T_0 see Eq. (9) and Sec. VII]. While for $U/\Gamma_0 < 7$, where high- and low-temperature scales are not very well separated, the maximum of the resistivity and the peak height show a U dependence, we reach a universality regime for large U . Note that T_0 is of the order of the position T_{max} of the maximum of the resistivity while the T^2 behavior of the resistivity is only observed below the coherent scale T_{cor} which is two orders of magnitude smaller.

The dependence of the resistivity $\rho(T)$ on the total occupation n_{tot} is shown in Fig. 11 for fixed $U/\Gamma_0 = 10$ and $\varepsilon_f - \varepsilon_c = -U/2$. We see that the (artificial) residual resistivity $\rho(0)$ increases whereas the maximum temperature T_{max} decreases when approaching the Kondo insulator regime at $n_{\text{tot}} = 2$ (symmetric PAM). In this case $\rho(T)$ saturates for $T < 10^{-2}$, which is typical for Kondo insulators.³ Experimentally, this is due to impurities; in our calculations it is a consequence of the finite-energy imaginary part δ . For fixed $n_{\text{tot}} = 2$ and different values of $\varepsilon_f - \varepsilon_c$, $\rho(T)$ is shown in Fig. 12; obviously, the Kondo insulator behavior is not only obtained in the symmetric case but always for $n_{\text{tot}} = 2$ in accordance with the Luttinger theorem. The (artificial) finite $\rho(0)$ depends hardly on $\varepsilon_f - \varepsilon_c$ but only on the finite δ .

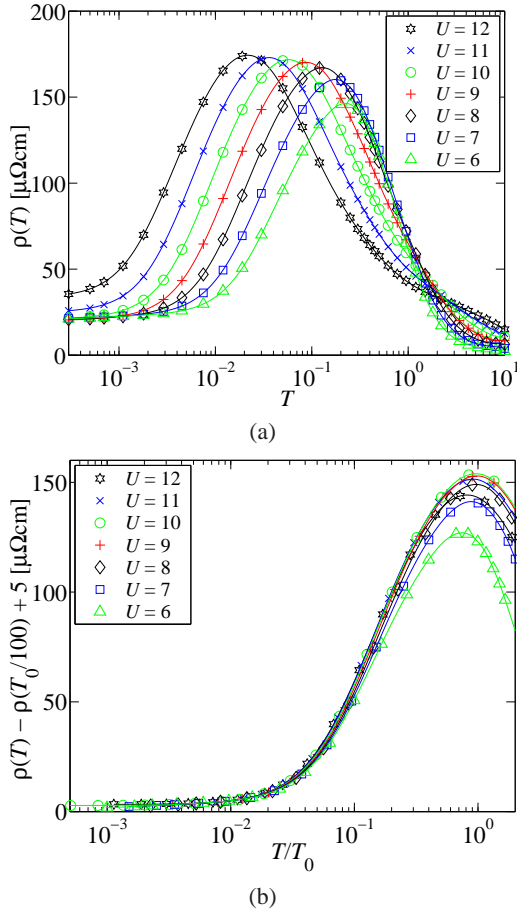


FIG. 10: (Color online) Resistivity $\rho(T)$ as function of T for different U , $\varepsilon_f - \varepsilon_c = -U/2$, and fixed total filling $n_{\text{tot}} = 1.6$. The calculations were done in DMFT-NRG, thus continuing the NRG series of Fig. 9 to higher U . NRG Parameters: as in Fig. 1. In (b) the same data is plotted as $\rho(T) - \rho(T_0/100) + 5 \mu\Omega\text{cm}$ versus T/T_0 with T_0 as in Eq. (9).

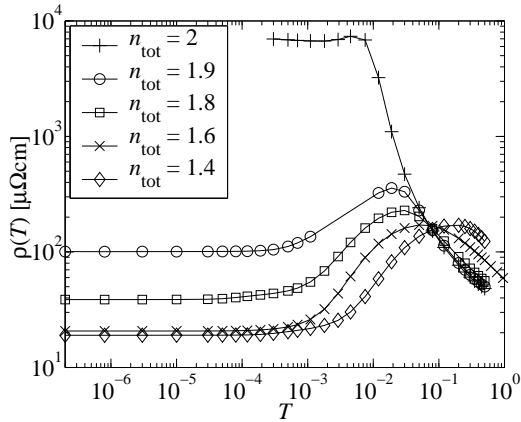


FIG. 11: Resistivity $\rho(T)$ for different total fillings n_{tot} , $U/\Gamma_0 = 10$, $\varepsilon_f - \varepsilon_c = -U/2$, $\delta/\Gamma_0 = 10^{-3}$. NRG parameters: as in Fig. 1.

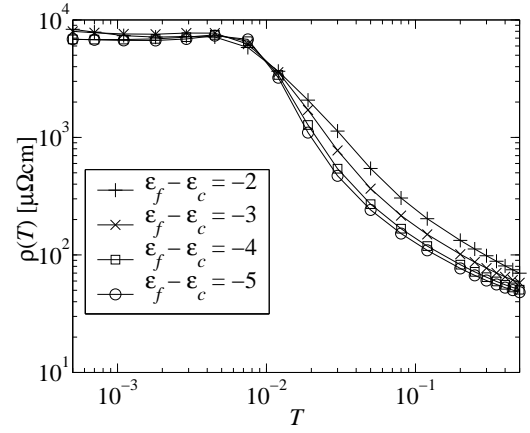


FIG. 12: Resistivity $\rho(T)$ for different $\varepsilon_f - \varepsilon_c$, $\delta/\Gamma_0 = 10^{-3}$, $U/\Gamma_0 = 10$, $n_{\text{tot}} = 2$ (Kondo insulators). NRG parameters: as in Fig. 1.

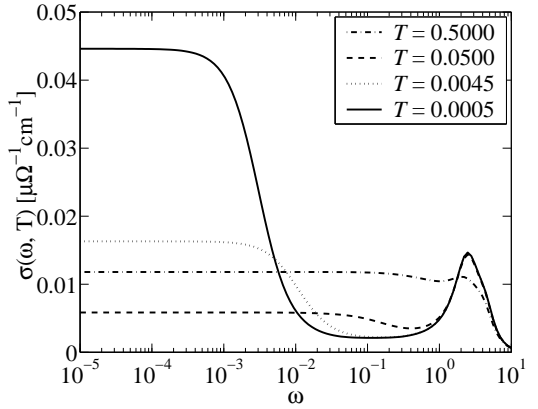


FIG. 13: Optical conductivity for four different temperatures $T \approx 0.01, 0.1, 1, 10T_{\text{max}}$, $n_{\text{tot}} = 1.6$, and a fixed $U/\Gamma_0 = 10$, $\varepsilon_f - \varepsilon_c = -U/2$. NRG parameters: as in Fig. 1.

B. Optical conductivity

The optical conductivity $\sigma(\omega)$ obtained in the metallic case for $n_{\text{tot}} = 1.6$ is shown in Fig. 13 for different temperatures T . For very low T one observes a Drude peak at low frequencies and, in addition, a "midinfrared" peak at finite frequency $\omega \sim \sqrt{t^* T_0}$. With increasing T the Drude peak quickly decreases (in accordance with the strong increase of the static resistivity), whereas the midinfrared peak remains nearly unchanged, and the remainders of the Drude peak and the midinfrared peak merge into a broad structure in the high temperature regime.

Figure 14 shows $\sigma(\omega)$ for a Kondo insulator, where for very low T the Drude peak is absent and only the midinfrared peak is present due to interband transitions. With increasing T , however, the gap disappears, and the metallic heavy-fermion behavior at high temperatures is recovered.

This behavior can easily be understood in terms of the renormalized bands discussed in Sec. III and shown in Fig. 6.

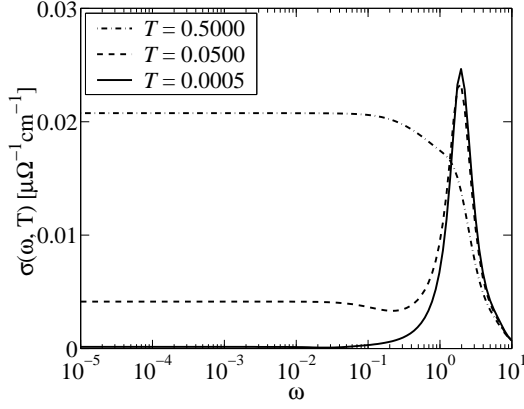


FIG. 14: Optical conductivity for three different temperatures T , $n_{\text{tot}} = 2$ (i.e., Kondo insulators), and a fixed $U/\Gamma_0 = 10$, $\epsilon_f - \epsilon_c = -U/2$. NRG parameters: as in Fig. 1.

With the assumption of a constant density of states $\rho_0(\mu)$, $\sigma(\omega)$ can be approximated by

$$\frac{\sigma(\omega)}{\sigma_0} = \frac{i\rho_0(\mu)}{2\omega} \int_{-\infty}^{\infty} \frac{d\omega' [f(\omega') - f(\omega' + \omega)]}{\omega + \Sigma^c(\omega' - i\delta) - \Sigma^c(\omega' + \omega + i\delta)}. \quad (34)$$

The optical conductivity $\sigma(\omega)$ has a maximum when the real part of the denominator on the right-hand side of Eq. (34) vanishes.⁷⁶ This is obviously the case for $\omega \rightarrow 0$ for metallic HFSs in the Fermi-liquid regime, which yields the Drude peak. An additional maximum is found in the vicinity of the minimal intraband transition energy close to the chemical potential, which yields the midinfrared peak. An estimate for its position is the smallest interband transition energy for $\vec{q} = 0$ given by $\Delta_{\text{opt}} \propto \sqrt{t^* T_0}$ which fits perfectly with the observed midinfrared peak of a large variety of different heavy-fermion compounds.²² Its temperature dependence is weak since the spectral weight moved from lower to higher excitation energies is small. On the other hand, the midinfrared peak width depicted in Fig. 13 and reported in Ref. 76 comes out much narrower than the experimentally observed peaks.⁶⁶ This is expected because in real materials, all Hund's-rule multiplets contribute to the scattering of the conduction electrons in the midinfrared region. Our simplified model, however, only contains the lowest Hund's-rule doublet. The total optical response is furnished by a superposition of all scattering resonances which leads to an effectively broad resonance as observed experimentally.

C. Thermoelectricity

The thermoelectric power $S(T)$ measures the ratio between electrical and heat current divided by the temperature, and its sign is related to the integrated particle-hole asymmetry relative to the chemical potential. In Fig. 15, $S(T)$ is plotted for $\epsilon_f - \epsilon_c = -U/2$ and fixed total filling for a variety of different values of U [for the low-temperature scale T_0 see Eq. (9) and Sec. VII]. We obtain very large absolute values for $S(T)$,

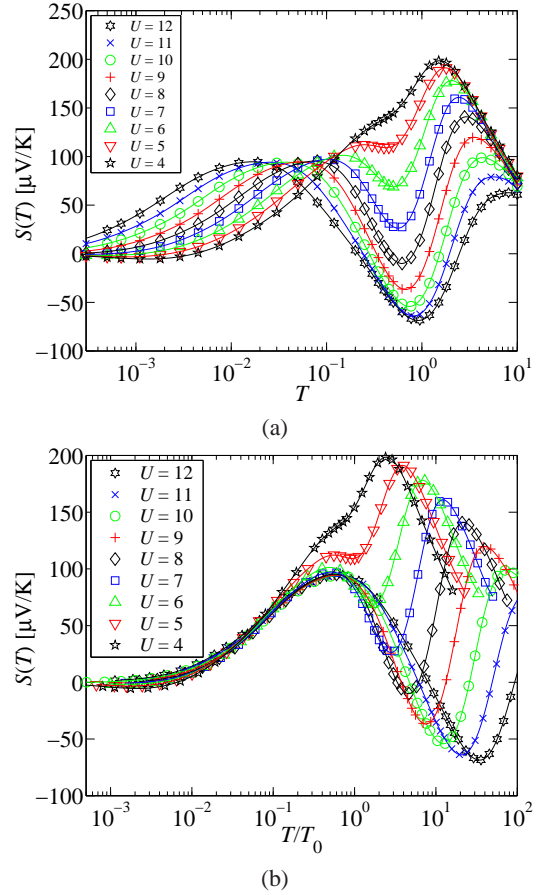


FIG. 15: (Color online) Thermoelectric power for various values of U and fixed total occupation $n_{\text{tot}} = 1.6$ and $\epsilon_f - \epsilon_c = -U/2$. Panel (b) shows the same data but on a rescaled axis T/T_0 with T_0 as in Eq. (9). All Parameters: as in Fig. 10.

of the magnitude $50 \mu\text{V/K}$ up to $150 \mu\text{V/K}$; note that the thermoelectric power is obtained in absolute units, as already mentioned in Sec. IV. Similar to the resistivity, the thermoelectric power exhibits a low-temperature peak which is correlated with the maximum of the resistivity which is an analytical consequence of Eq. (29). In addition, we observe a second extremum moving to higher temperatures with increasing U which results from the charge fluctuations on the energy scale $\epsilon_f - \mu$.

It is very interesting to note that for $U/\Gamma_0 > 8$ the thermoelectric power changes sign in an intermediate-temperature regime. Several extrema and similar sign changes were found experimentally for several HFS materials, in particular below 80 K for $\text{CeCu}_{2.2}\text{Si}_2$.^{77,78} As we have discussed in Sec. III, the details of the spectrum close to the hybridization gap depend on the free single-particle DOS $\rho_0(\omega)$. In addition, our model does not include other Hund's-rule multiplets. Therefore, we only can make a qualitative comparison with experiments. Remarkably, however, we find a sign change of the thermoelectric power for large U and a large absolute value of $S(T)$ comparable to the experimental results.

The thermoelectric power $S(T)$ for different fillings n_{tot} ,

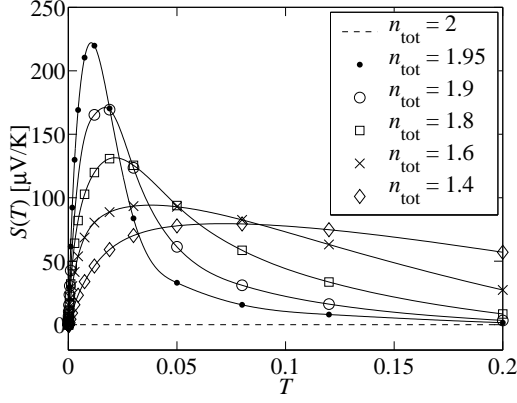


FIG. 16: Thermoelectric power for a fixed $U/\Gamma_0 = 10$ and various occupations $n_{\text{tot}} = 1.4, 1.6, 1.9, 1.95, 2$ and $\epsilon_f - \epsilon_c = -U/2$. All parameters: as in Fig. 11.

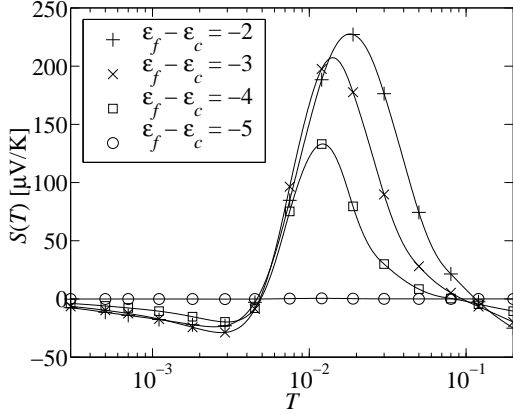


FIG. 17: Thermoelectric power for $U/\Gamma_0 = 10$, $n_{\text{tot}} = 2$ (Kondo insulator regime) and different values for ϵ_f (or $\epsilon_f - \epsilon_c$). All parameters: as in Fig. 12.

$U/\Gamma_0 = 10$, and $\epsilon_f - \epsilon_c = -U/2$ is depicted in Fig. 16. For $n_{\text{tot}} = 2$ the thermoelectric power vanishes for all temperatures because of particle-hole symmetry. Otherwise $S(T)$ exhibits a peak with increasing height when approaching the Kondo insulator regime $n_{\text{tot}} \rightarrow 2$. For the Kondo insulator situation $n_{\text{tot}} = 2$ and various $\epsilon_f - \epsilon_c$ the thermoelectric power $S(T)$ is shown in Fig. 17. Only in the symmetric case $\epsilon_f = -U/2 = -5\Gamma_0$ does $S(T)$ vanish due to particle hole symmetry; away from the symmetric case, the peaks reach extremely large absolute values of S up to $200 \mu\text{V/K}$. This shows that Kondo insulators could be candidates for thermoelectric applications.

However, the figure of merit $Z = S^2\sigma/\kappa$, or the dimensionless value ZT and not only the Seebeck coefficient $S(T)$ is of relevance for efficient thermoelectric cooling, where κ is the thermal conductivity. Since approaching the Kondo insulator reduces the conductivity σ as well as shifting the peak to very low temperatures the nominator of ZT will be rather small. Fig. 18 shows the electronic part of the thermal conductivity $\kappa(T)$. As expected $\kappa(T)$ is rapidly increasing with

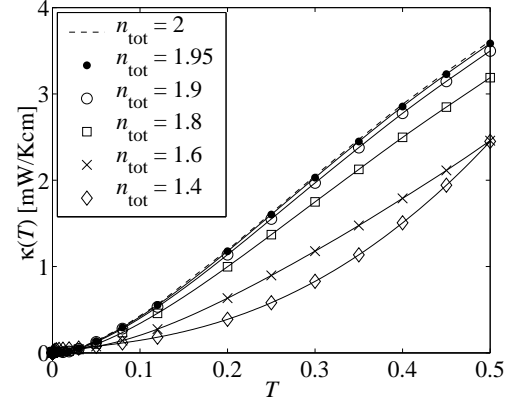


FIG. 18: Electronic part of thermal conductivity for $U/\Gamma_0 = 10$, $\epsilon_f - \epsilon_c = -U/2$. All parameters: as in Figs. 11 and 16.

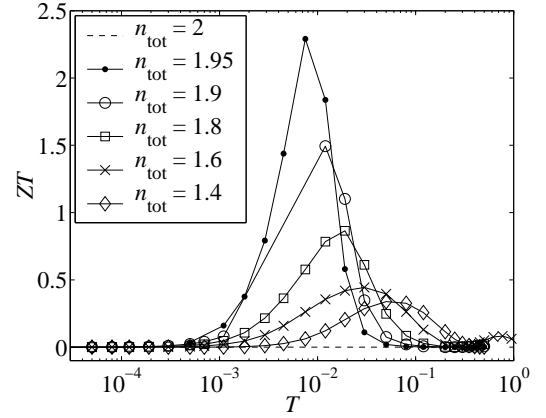


FIG. 19: Figure of merit for $U/\Gamma_0 = 10$, $\epsilon_f - \epsilon_c = -U/2$. All parameters: as in Figs. 11 and 16.

increasing T and the overall behavior is similar as that observed experimentally.¹⁵

The resulting temperature dependence of the figure of merit is shown in Fig. 19. According to our calculations a figure of merit larger than 1 can be obtained in HFSs in certain low-temperature regimes, showing that, in fact, they are candidates for thermoelectric applications.

VI. LOW-TEMPERATURE SCALES

There has been a long debate whether low-temperature properties are governed by one or more low-energy scales in the paramagnetic phase of the PAM.^{36,45,76,79,80} In the SIAM, the screening of the local moments occurs on the scale of Kondo temperature T_K where the system crosses over from the local-moment to the strong-coupling fixed point when lowering the temperature. But Nozières has argued that for the lattice with a macroscopic concentration of f moments there is an “exhaustion” of the conduction electrons^{79,80} available for screening of those f moments. However, it is questionable whether the concept of individually screened indepen-

dent single impurities still holds in a lattice, because one conduction electron could rather contribute to the screening of several local moments. In this context, it has been suggested that two different low-temperature scales exist in the paramagnetic phase of the PAM: namely, the single-impurity Kondo scale T_K and a strongly reduced lattice scale $T_{\text{low}} \ll T_K$ at which the screening of the local moments happens. It was argued that at T_K only $n_{\text{scr}} = \rho_c(0)T_K$ conduction electrons are available to screen n_f local f electrons, where $\rho_c(0)$ is the conduction-electron DOS at the chemical potential. However, in Nozières's work⁷⁹ only phenomenological estimates and no precise mathematical definitions for different temperature scales are given.

It is tempting to identify the possibly existing additional scale T_{low} with the “coherence temperature”—i.e., the scale on which the heavy quasiparticles are formed and/or on which the T^2 behavior in the resistivity is observable. Experimentally, however, no evidence was found for such a large separation of energy scales in heavy-fermion compounds.^{1,2} On the contrary, substitution of Ce by La in $\text{Ce}_{1-x}\text{La}_x\text{Cu}_6$ exhibits nearly perfect scaling of the Ce contribution to the specific heat¹⁹ from the diluted impurity situation ($x \approx 1$) to the lattice case ($x = 0$) indicating that there is only one relevant energy scale. Recent theoretical investigations by Vidhyadhiraja and Logan gave evidence for such a single low-temperature scale,^{43,44,45} using Fermi-liquid assumptions for the f -electron self-energy. Their arguments are consistent with the notion that a new thermodynamically relevant energy scale can only occur as crossover scale from competing low-temperature fixed points. Our NRG calculations for the effective site, moreover, gave no evidence for new fixed points of the SIAM other than those already discussed in Ref. 57. In fact, we always find a strong-coupling fixed point independent of the filling connecting Kondo insulators adiabatically to metallic heavy-fermion systems.

In the literature, different notions of what is implied by the term “low-temperature scale” have led to a controversy which could have been resolved by stating clearly the precise mathematical definitions of such distinct scales. The low-temperature scale T_{low} allows to map any temperature-dependent property $P(T)$ over a limited low-temperature range⁴⁴ onto a corresponding dimensionless universal function $p(x = T/T_{\text{low}})$ where all details of the initial microscopic Hamiltonian enter this single scale T_{low} . From a renormalization group perspective, it describes the crossover from one fixed point to the $T = 0$ fixed point. If such a quantity P has distinct analytical behavior in different temperature intervals, it is tempting to assign additional low-temperature scales to identify such different regimes. If, however, a universal function $p(x)$ can be found such that $P(T)$ collapses onto this curve for all low-temperature regimes, these distinct scales contain no additional physical information. The confusion in the literature arises by ignoring that these admittedly different low-temperature scales might ultimately be connected and reflect the same physical phenomena. If, however, different scaling regimes can be identified using two or more low-temperature scales, it should correspond to additional fixed points of the Hamiltonian.

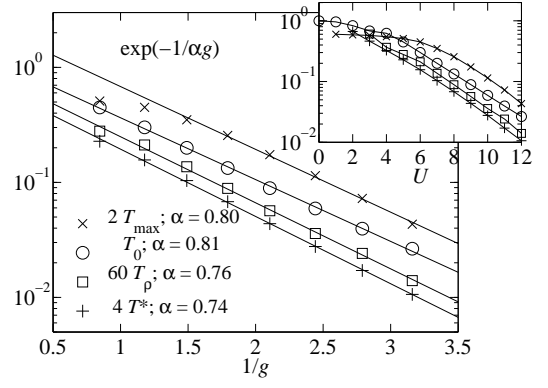


FIG. 20: The four different low-temperature scales plotted versus the reciprocal dimensionless coupling constant $1/g$ [cf. Eq. (35)]. The inset shows the same data as function of U . The stars mark the maximum of the resistivity T_{max}/Γ_0 the crosses the screening of the spin moment of the effective site. The squares indicate $T_\rho = 1/\sqrt{\sigma_0 A}$, while the mass enhancement factor is plotted by the circles. Parameters: $\varepsilon_f - \varepsilon_c = -U/2$, $n_{\text{tot}} = 1.6$, number of retained NRG states $N_s = 1500$, $\Lambda = 1.6$, $\delta/\Gamma_0 = 10^{-3}$.

A. Definition of different low-temperature scales

From our data, we have defined *four different* possible low-temperature scales characterizing *different* physical phenomena in order to identify more than one low-temperature scale. These scales are (i) the low-temperature scale⁴⁴ $T_0 = \Gamma_0 m/m^*$, Eq. (9), defined by the quasiparticle spectral weight, measuring the reciprocal mass enhancement m/m^* for $T \rightarrow 0$,

$$m/m^* = \left[1 - \frac{\partial \text{Re} \Sigma^f(\omega)}{\partial \omega} \Big|_{\omega, T \rightarrow 0} \right]^{-1};$$

(ii) the A coefficient of the resistivity $\rho(T) = \rho_0 + AT^2$ valid in the coherent Fermi-liquid regime, $T_\rho = (\sigma_0 A)^{-1/2}$, where σ_0^{-1} is the natural unit of the resistivity given in Eq. (31); (iii) the position of the maximum of the resistivity curve T_{max} for metallic heavy-fermion systems; and (iv) the screening temperature T^* of the impurity moment³³ $\langle S_z^2 \rangle_{\text{imp}}(T^*) = 0.05$.

Other possible scales such as the width of the hybridization gap are not very well defined since the position and depth of the gap as well as the shape of the spectral function are strongly dependent on the Fermi volume. In the following, we will show that all scales are connected by a fixed ratio when varying the interaction strength U for fixed occupancy n_{tot} or Fermi volume.

The mass enhancement factor m^*/m as well as the A coefficient of the resistivity contains information on the low-lying excitations of the lattice Fermi-liquid fixed point as pointed out by Logan and collaborators.⁴⁴ Both should be proportional to a low-temperature scale T_{low} . We contrast this with two estimates of a possible second low-temperature scale. It was argued that this scale governs the crossover from a regime of incoherent scattering of the conduction electrons to a coherent Fermi-liquid ground state of the lattice.³⁶ This truly new scale would mark the deviation of a periodic Anderson model

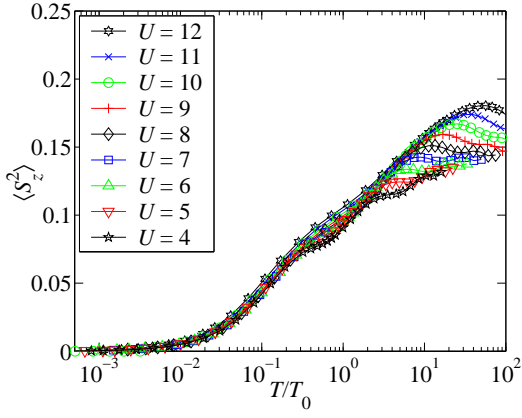


FIG. 21: (Color online) The temperature dependence of the effective moment $\langle S_z^2 \rangle_{\text{imp}}(T)$ versus T/T_0 for various values of U and a fixed filling of $n_{\text{tot}} = 1.6$. Parameters: as in Fig. 20.

from the properties of the SIAM. We take the position of the maximum of the resistivity T_{max} as one clear indicator of such a scale as well as the screening of the impurity effective moments which defines the temperature T^* . However, we like to point out that our definitions of the low-temperature scales do not imply an energy hierarchy $T_0 < T_{\text{max}}$.

B. Discussion of the scales

Using Wilson's definition³³ of an effective local moment, $\langle S_z^2 \rangle_{\text{imp}}(T)$ is given by the difference of $\langle S_z^2 \rangle$ of the effective SIAM and the medium electron gas without impurity. Since the medium changes with temperature, $\langle S_z^2 \rangle_{\text{imp}}(T)$ is calculated for each converged medium for the given temperature and T^* is obtained by the condition $\langle S_z^2 \rangle_{\text{imp}}(T^*) = 0.05$.

The results for all four different scales are depicted in Fig. 20 using a fixed filling $n_{\text{tot}} = 1.6$. While the fit to the T^2 behavior contains a significant error bar due to the logarithmic temperature scale of the NRG and the limited temperature range of the Fermi-liquid regime, all other energy scales can be obtained with high accuracy due to their definition. The dimensionless coupling constant

$$g = \rho_0 J = \frac{2\Gamma_0 U}{\pi|\epsilon_f| + U} \quad (35)$$

has been estimated by the Schrieffer-Wolff transformation.⁸¹ All four scales show the same exponential dependency on U with $T_0 \propto \exp(-1/\alpha g)$ with $\alpha \approx 0.8$ for large U where the charge and low-temperature scales are well separated. This indicates that, up to a filling-dependent proportionality constant, there exists only *one* low-temperature scale. Our findings are in perfect agreement with the previously reported³⁶ $T = 0$ estimates of the low-temperature scale but in contrast to the Gutzwiller results⁸² predicting an enhancement of the $T_0/T_K = \exp(1/2g)$. However, the latter ratio is strongly filling dependent as pointed out previously.³⁶

As a consequence of this scaling analysis, $\langle S_z^2 \rangle_{\text{imp}}(T)$ is collapsed onto one master curve for a fixed filling n_{tot} and

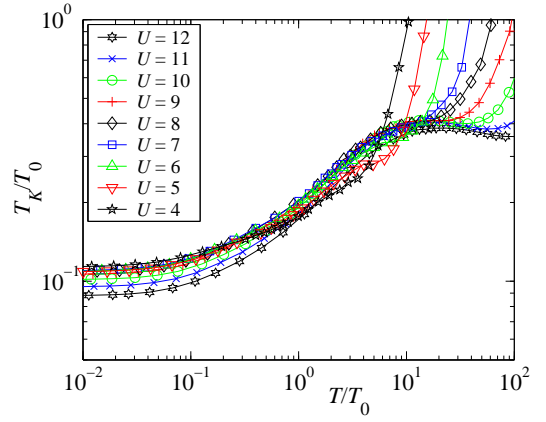


FIG. 22: (Color online) The temperature-dependent Kondo temperature $T_K(T)$ of the effective site for various U plots versus the scaling variable $x = T/T_0$ for fixed filling. Parameters: as in Fig. 21.

different values of U using the scaling variable $x = T/T_0$ as displayed in Fig. 21. This master curve for $\langle S_z^2 \rangle_{\text{imp}}(T)$ shows slight deviation from its corresponding shape for the SIAM with constant density of states,⁵⁷ however, it holds up to very high temperatures. Clearly visible is the U dependence of the maximum of $\langle S_z^2 \rangle_{\text{imp}}(T)$. Only in the local moment fixed point the value of $\langle S_z^2 \rangle_{\text{imp}} = 0.25$ is reached.⁵⁷ At high temperatures, deviations from scaling are related to the crossover from the free orbital to the local-moment fixed point⁵⁷ and are independent of lattice renormalization effects.

In addition, we can define a “temperature” dependent Kondo scale $T_K(T)$ of the DMFT effective site, by taking the DMFT medium density of states $\rho_{\text{eff}}(\omega)$ for a fixed temperature and solving the condition $\langle S_z^2 \rangle_{\text{imp}}(T_K) = 0.05$ for such a fixed medium. Since we would find a constant $T_K(T)$ for a SIAM, deviations from such a constant function indicate lattice renormalization effects. This also could give strong hints towards the existence of a second low-energy scale. $T_K(T \rightarrow \infty)$ corresponds to a “free-impurity” Kondo temperature. In the Fermi-liquid regime, $T_K(T)$ approaches a constant $T_K(0)$ measuring the lattice low-temperature scale: $T_K(0) \sim T_0$. In Fig. 22, the resulting renormalized dimensionless Kondo temperature $T_K(T)/T_0$ is plotted versus T/T_K for different values of U . Even though two distinguishable plateaus are visible, indicating two different low-temperature scales for large values of U , they are connected by a fixed ratio independent of U .

The existence of such universal scaling curves for $\langle S_z^2 \rangle_{\text{imp}}$ and $T_K(T)$ connecting these different temperature regimes provides strong evidence that (i) the low-temperature phase of the paramagnetic PAM is characterized by only one thermodynamic low-temperature scale, and (ii) all additionally defined low-energy scales assigned to features of some physical properties are proportional to this single low-temperature scale. Our findings are in agreement with the previous DMFT-NRG study³⁶ as well as the series of DMFT-LMA investigations of scaling and transport properties.^{43,44,45} We did not find any indication for a novel fixed point of the effective site introduced

by the nonconstant density of states. In the absence of a phase transition, the effective site is characterized by the same fixed points as the SIAM⁵⁷ and, therefore, only one universal low-temperature scale is expected.

VII. CONCLUSION AND OUTLOOK

We presented a comprehensive study of the transport properties of the periodic Anderson model. We calculated the resistivity and the thermoelectric power for metallic heavy-fermion systems as well as Kondo insulators using finite temperature DMFT-NRG and DMFT-MPT approaches. While the DMFT-MPT gives extremely reliable results in the weak correlation limit $\rho(0)U \ll 1$, it fails to reproduce the correct low-energy scale for large values of U . In contrast, the DMFT-NRG resolves accurately low-energy scales for arbitrary parameters but provides limited spectral resolution in finite-temperature spectral functions. The latter has made it very challenging to obtain reliable transport properties since only excitations of the order T enter the transport integrals. Nevertheless, we were able to use DMFT-NRG for the investigation of transport properties as well as the four different low-energy scales. All these energy scales are related by a fixed but filling-dependent ratio, indicating the existence of only one relevant low-temperature scale.

We conclude that all characteristic low-temperature transport properties of heavy-fermion systems can be explained within our numerical DMFT-NRG treatment of the PAM. In the metallic situation one obtains a low residual resistivity $\rho(0)$, a $\rho(T)$ rapidly increasing with increasing temperature T following a T^2 behavior for very low $T < T_0$, a maximum of the order $100 \mu\Omega \text{ cm}$ at a temperature T_{max} (about 10–200 K) and a $\rho(T)$ logarithmically decreasing with increasing T for $T > T_{\text{max}}$, thus showing the typical experimental behavior.^{17,18,19} At the same time the thermoelectric power can exhibit several extrema, for some parameters a change of sign, and large absolute values of the magnitude of 50–150 $\mu\text{V/K}$, as seen in experiments.^{77,78} The optical conductivity shows a Drude peak and an additional midinfrared peak for low T , whereas these structures merge to a broad structure at high T . For Kondo insulators a crossover from the Kondo behavior at $T > T_{\text{max}}$ to an activation behavior is obtained for $\rho(T)$ with a saturation due to the (artificial) finite imaginary

part δ (simulating impurity scattering), and the optical conductivity has no Drude peak for very low T . The absolute value of the thermoelectric power $S(T)$ can be even larger in or close to the Kondo insulator situation reaching giant values of more than 200 $\mu\text{V/K}$. The figure of merit can be larger than 1, showing that these systems are candidates for thermoelectric applications.

Thus far all our calculations did not include orbital degeneracy which is subject to crystal electric field splittings. These additional degrees of freedom are essential for the understanding of the transport properties of heavy-fermion systems in the intermediate temperature regime⁷⁸ as well as the broad midinfrared peak observed in the optical conductivity.⁶⁶ As recently pointed out,^{27,83,84} these additional f configurations can indeed introduce additional low-energy scales due to competition or crossover between additional fixed points. Apparently, the thermoelectric power is very sensitive to such additional configurations since it is determined by particle-hole asymmetry around the chemical potential.

Therefore, in the future this work can and should be extended into different directions. On the one hand, the inclusion of realistic f -shell degeneracy and of crystal fields is highly desirable to come to a more realistic description of the transport properties of heavy-fermion systems valid also for high T , where the higher crystal field levels can be excited. On the other hand, the influence of disorder and alloying, in particular of the substitution of the (magnetic) lanthanide or actinide ions by nonmagnetic ions should be investigated and understood theoretically, as there exist many experimental investigations systematically studying these substitution effects.

Note added in proof. After completion of this work, potentially more accurate ways of calculating the NRG spectral functions were proposed^{64,65} which might increase the accuracy of future DMFT-NRG calculations.

Acknowledgments

We thank A. Hewson, J. Freericks, D. Logan, R. Bulla, N. Grewe, and V. Zlatić for numerous discussions. C.G., F.B.A., and G.C. acknowledge financial support by the Deutsche Forschungsgemeinschaft, Project No. AN 275/5-1 and funding of the NIC, Forschungszentrum Jülich, under Project No. HHB000.

- ¹ N. Grewe and F. Steglich, in *Handbook on the Physics and Chemistry of Rare Earths*, edited by K. A. Gschneidner, Jr. and L. Eyring (North-Holland, Amsterdam, 1991), Vol. 14, p. 343.
- ² G. R. Stewart, *Rev. Mod. Phys.* **73**, 797 (2001).
- ³ M. F. Hundley, P. C. Canfield, J. D. Thompson, Z. Fisk, and J. M. Lawrence, *Phys. Rev. B* **42**, 6842 (1990).
- ⁴ F. Steglich, J. Aarts, C. D. Bredl, W. Lieke, D. Meschede, W. Franz, and H. Schäfer, *Phys. Rev. Lett.* **43**, 1892 (1979).
- ⁵ W. P. Beyermann, M. F. Hundley, P. C. Canfield, J. D. Thompson, Z. Fisk, J. L. Smith, M. Selsane, C. Godart, and M. Latroche, *Phys. Rev. Lett.* **66**, 3289 (1991).

- ⁶ A. Loidl, A. Krimmel, K. Knorr, G. Sparr, M. Lang, C. Geibel, S. Horn, A. Grauel, F. Steglich, B. Welslau, et al., *Ann. Phys. (Leipzig)* **1**(2), 78 (1992).
- ⁷ N. Grewe, Th. Pruschke, and H. Keiter, *Z. Phys. B: Condens. Matter* **71**, 75 (1988).
- ⁸ N. Grewe and B. Welslau, *Solid State Commun.* **65**, 437 (1988).
- ⁹ F. B. Anders, *Phys. Rev. Lett.* **83**, 4638 (1999).
- ¹⁰ F. Steglich, in *Festkörperprobleme: Advances in Solid State Physics*, edited by J. Treusch (Vieweg, Braunschweig, 1977), Vol. 17, p. 319.
- ¹¹ H. Schneider, Z. Kletowski, F. Oster, and D. Wohlleben, *Solid*

- State Commun. **48**, 1093 (1983).
- 12 D. Jaccard, J. M. Mignot, B. Bellarbi, A. Benoit, H. F. Braun, and J. Sierro, *J. Magn. Magn. Mat.* **47–48**, 23 (1985).
 - 13 D. Jaccard, A. Basset, J. Sierro, and J. Pierre, *J. Low Temp. Phys.* **80**, 285 (1990).
 - 14 M. Očko, B. Bushinger, C. Geibel, and F. Steglich, *Physica B* **259–261**, 87 (1999).
 - 15 S. Paschen, B. Wand, G. Sparn, F. Steglich, Y. Echizen, and T. Takabatake, *Phys. Rev. B* **62**, 14912 (2000).
 - 16 G. Mahan, B. Sales, and J. Sharp, *Phys. Today* **50**(3), 42 (1997).
 - 17 P. Scoboria, J. E. Crow, and T. Mihalisin, *J. Appl. Phys.* **50**, 1895 (1979).
 - 18 K. Andres, J. E. Graebner, and H. R. Ott, *Phys. Rev. Lett.* **35**, 1779 (1975); H. R. Ott, H. Rudigier, Z. Fisk, J. L. Smith, *Physica B* **127**, 359 (1984).
 - 19 Y. Onuki and T. Komatsubara, *J. Magn. Magn. Mat.* **63–64**, 281 (1987).
 - 20 Th. Pruschke, M. Jarrell, and J. K. Freericks, *Adv. Phys.* **42**, 187 (1995).
 - 21 A. Georges, G. Kotliar, W. Krauth, and M. J. Rozenberg, *Rev. Mod. Phys.* **68**, 13 (1996), for a review on the DMFT.
 - 22 L. Degiorgi, F. B. Anders, and G. Grüner, *Eur. Phys. J. B* **19**, 167 (2001).
 - 23 M. B. Maple, M. C. de Andrade, J. Herrmann, Y. Dalichaouch, D. A. Gajewski, C. L. Seaman, R. Chau, R. Movshovich, M. C. Aronson, and R. Osborn, *J. Low Temp. Phys.* **99**, 223 (1995).
 - 24 H. von Löhneysen, *J. Phys.: Condens. Matter* **8**, 9689 (1996).
 - 25 A. J. Millis, *Phys. Rev. B* **48**, 7183 (1993).
 - 26 S. Sachdev, *Quantum Phase Transitions* (Cambridge Press, Cambridge UK, 2001).
 - 27 F. B. Anders and Th. Pruschke, *Phys. Rev. Lett.* **96**, 086404 (2006).
 - 28 S. Doniach, *Physica B & C* **91**, 231 (1977).
 - 29 P. W. Anderson, *Phys. Rev.* **124**, 41 (1961).
 - 30 M. Jarrell, *Phys. Rev. Lett.* **69**, 168 (1992).
 - 31 A. Georges and G. Kotliar, *Phys. Rev. B* **45**, 6479 (1992).
 - 32 W. Metzner and D. Vollhardt, *Phys. Rev. Lett.* **62**, 324 (1989).
 - 33 K. G. Wilson, *Rev. Mod. Phys.* **47**, 773 (1975).
 - 34 A. Martín-Rodero, E. Louis, F. Flores, and C. Tejedor, *Phys. Rev. B* **33**, 1814 (1986).
 - 35 M. Pothoff, T. Wegner, and W. Nolting, *Phys. Rev. B* **55**, 16132 (1997).
 - 36 Th. Pruschke, R. Bulla, and M. Jarrell, *Phys. Rev. B* **61**, 12799 (2000).
 - 37 J. E. Hirsch and R. M. Fye, *Phys. Rev. Lett.* **56**, 2521 (1986).
 - 38 N. Grewe, *Z. Phys. B: Condens. Matter* **52**, 193 (1983).
 - 39 Y. Kuramoto, *Z. Phys. B: Condens. Matter* **53**, 37 (1983).
 - 40 N. E. Bickers, *Rev. Mod. Phys.* **59**, 845 (1987).
 - 41 A. Lorek, N. Grewe, and F. B. Anders, *Solid State Commun.* **78**, 167 (1991).
 - 42 F. B. Anders and D. L. Cox, *Physica B* **230–232**, 441 (1997).
 - 43 N. S. Vidhyadhiraja, V. E. Smith, D. E. Logan, and H. R. Krishnamurthy, *J. Phys.: Condens. Matter* **15**, 4045 (2003).
 - 44 N. S. Vidhyadhiraja and D. E. Logan, *Eur. Phys. J. B* **39**, 313 (2004).
 - 45 D. E. Logan and N. S. Vidhyadhiraja, *J. Phys.: Condens. Matter* **17**, 2935 (2005); N. S. Vidhyadhiraja and D. E. Logan, *ibid.* **17**, 2959 (2005).
 - 46 T. A. Costi and N. Manini, *J. Low Temp. Phys.* **126**, 835 (2002).
 - 47 I. N. Karnaukhov, *Phys. Rev. B* **56**, R4313 (1997).
 - 48 H. Keiter and J. C. Kimball, *Int. J. Magn.* **1**, 233 (1971).
 - 49 Y. Kuramoto, in *Theory of Heavy Fermions and Valence Fluctuations*, edited by T. Kasuya and T. Saso (Springer Verlag, Berlin, 1985), p. 152.
 - 50 C. I. Kim, Y. Kuramoto, and T. Kasuya, *Solid State Commun.* **62**, 627 (1987).
 - 51 N. Grewe, *Z. Phys. B: Condens. Matter* **67**, 323 (1987).
 - 52 C. I. Kim, Y. Kuramoto, and T. Kasuya, *J. Phys. Soc. Jpn.* **59**, 2414 (1990).
 - 53 E. Müller-Hartmann, *Z. Phys. B: Condens. Matter* **76**, 211 (1989).
 - 54 U. Brandt and C. Mielsch, *Z. Phys. B: Condens. Matter* **75**, 365 (1989).
 - 55 H. Schweitzer and G. Czycholl, *Solid State Commun.* **74**, 735 (1990); *Z. Phys. B: Condens. Matter* **83**, 83 (1991).
 - 56 F. B. Anders, *Eur. Phys. J. B* **28**, 9 (2002).
 - 57 H. R. Krishna-murthy, J. W. Wilkins, and K. G. Wilson, *Phys. Rev. B* **21**, 1003 (1980); **21**, 1044 (1980).
 - 58 R. Bulla, Th. Pruschke, and A. C. Hewson, *J. Phys.: Condens. Matter* **9**, 10463 (1997).
 - 59 F. B. Anders and G. Czycholl, *Phys. Rev. B* **71**, 125101 (2005).
 - 60 R. Bulla, T. A. Costi, and D. Vollhardt, *Phys. Rev. B* **64**, 045103 (2001).
 - 61 R. Bulla, A. C. Hewson, and Th. Pruschke, *J. Phys.: Condens. Matter* **10**, 8365 (1998).
 - 62 H. Schweitzer and G. Czycholl, *Solid State Commun.* **69**, 171 (1989).
 - 63 T. Costi, A. C. Hewson, and V. Zlatić, *J. Phys.: Condens. Matter* **6**, 2519 (1994).
 - 64 A. Weichselbaum and J. von Delft, cond-mat/0607497 (unpublished).
 - 65 R. Peters, Th. Pruschke, and F. B. Anders, cond-mat/0607494, *Phys. Rev. B* (to be published).
 - 66 L. Degiorgi, *Rev. Mod. Phys.* **71**, 697 (1999).
 - 67 J. M. Luttinger, *Phys. Rev.* **135**, A1505 (1964).
 - 68 G. Mahan, *Many-Particle Physics* (Plenum Press, New York, 1981).
 - 69 P. Voruganti, A. Golubentsev, and S. John, *Phys. Rev. B* **45**, 13945 (1992).
 - 70 G. Czycholl, *Theoretische Festkörperphysik* (Springer, Heidelberg, 2000).
 - 71 G. Czycholl and H. J. Leder, *Z. Phys. B: Condens. Matter* **44**, 59 (1981).
 - 72 A. Khurana, *Phys. Rev. Lett.* **64**, 1990 (1990).
 - 73 H. Schweitzer and G. Czycholl, *Phys. Rev. Lett.* **67**, 3724 (1991).
 - 74 D. L. Cox and N. Grewe, *Z. Phys. B: Condens. Matter* **71**, 321 (1988).
 - 75 Th. Pruschke, D. L. Cox, and M. Jarrell, *Europhys. Lett.* **21**, 593 (1993).
 - 76 M. Jarrell, *Phys. Rev. B* **51**, 7429 (1995).
 - 77 F. Steglich, B. Buschinger, P. Gegenwart, M. Lohmann, R. Helfrich, C. Langhammer, P. Hellmann, L. Donnevert, S. Thomas, A. Link, et al., *J. Phys.: Condens. Matter* **8**, 9909 (1996).
 - 78 F. B. Anders and M. Huth, *Eur. Phys. J. B* **19**, 491 (2001).
 - 79 P. Nozières, *Ann. Phys. (Paris)* **10**, 19 (1985); *Eur. Phys. J. B* **6**, 447 (1998).
 - 80 A. N. Tahvildar-Zadeh, M. Jarrell, Th. Pruschke, and J. K. Freericks, *Phys. Rev. B* **60**, 10782 (1999).
 - 81 J. R. Schrieffer and P. A. Wolff, *Phys. Rev.* **149**, 491 (1966).
 - 82 T. M. Rice and K. Ueda, *Phys. Rev. B* **34**, 6420 (1986).
 - 83 M. Koga and D. L. Cox, *Phys. Rev. Lett.* **82**, 2575 (1999).
 - 84 M. Koga, G. Zarand, and D. L. Cox, *Phys. Rev. Lett.* **83**, 2421 (1999).